THESIS

DEVELOPMENT AND CHARACTERIZATION OF A HIDDEN ANODE-BASED PLASMA CONTACTOR

Submitted by

Tait H. Freestone

Department of Mechanical Engineering

In partial fulfillment of the requirements

For the Degree of Master of Science

Colorado State University

Fort Collins, Colorado

Spring 2025

Master's Committee:

Advisor: John D. Williams

Azer Yalin
Jacob Roberts

ABSTRACT

DEVELOPMENT AND CHARACTERIZATION OF A HIDDEN ANODE-BASED PLASMA CONTACTOR

The use of high-current, high-energy electron beams on spacecraft can result in excessive positive electrostatic charging beyond passive mitigation capabilities, potentially terminating beam emission. To counteract this, active charge mitigation via positive ion emission is necessary. This thesis evaluates the Hidden Anode Plasma Contactor (HAPC), developed for the University of Michigan's Beam-Spacecraft Plasma Interaction and Charging Experiment (BSPICE), designed specifically for rapid start, active charge mitigation of a sounding rocket mission.

This study characterizes the plasma plume generated by the HAPC along with its operational characteristics, while also detailing the Krypton gas feed system and associated electronics. Ion current production required for the mission was verified through current density measurements and pulse bias testing. Measurements revealed a near-hemispherical plasma expansion, ion energy distributions resembling those of Hall thrusters, and predominant singly charged ions, though multiply charged ions were present. Langmuir probe analysis of the plasma plume downstream of the HAPC identified two distinct electron populations—thermal electrons and higher-energy primaries emitted directly from the cathode.

Anode orifice erosion at high power and expellant utilization above 10% was observed, which would likely limit the lifetime of the HAPC to tens of minutes—times much greater than the 7-minute typical duration of a sounding rocket mission. The findings provide comprehensive insights into HAPC operation for BSPICE and highlight its applicability as an alternative plasma source where Hall thruster-like plume characteristics are desired.

ACKNOWLEDGEMENTS

I would like to express my immense gratitude to Dr. John D. Williams, my advisor, for the opportunity to study in grad school under him, and for all the advice, guidance, support, and access to his great expertise and all his experience during my research and study. A great thank you also goes to my committee members, Dr. Azer Yalin and Dr. Jacob Roberts, for their input and advice on my thesis.

Special Thank you to Dr. Cody Farnell for the final layout of the printed circuit board for the krypton flow control board and advice and assistance given during our work together on the B-SPICE project.

Thank you as well to Dr. Shawn Farnell for the programming of the HAPC microcontroller, writing the program allowing the commanding of and data acquisition off of the HAPC microcontroller along with the probe analysis programs and all other help during the B-SPICE project.

Many thanks to Mr. Seth J. Thompson and Dr. Casey Farnell for their advice, assistance, mentorship, and support during my research and the development of the HAPC. And thank you to my fellow students in the lab at CEPPE for their support.

TABLE OF CONTENTS

Chapter 1 - Introduction

We will start this thesis with an introduction covering background information on spacecraft charging, electron-beam missions, and plasma sources for charge mitigation. This is to establish an understanding of the motivation behind the work of this thesis, which was to support the Beam-Spacecraft Plasma Interaction and Charging Experiment.

Section 1.1 - E-beams from spacecraft and spacecraft charging

A phenomenon important to spacecraft design is that of spacecraft charging. Spacecraft charging occurs when a spacecraft accumulates electric charge resulting in surface and frame potentials that are different than the ambient space plasma [1]. Typically charging occurs due to a difference in the initial flux of ions and electrons as electrons are much lower mass and move more quickly than ions. After the initial charge accumulation process finishes, the spacecraft surfaces and frame equilibrate at potentials such that the ion and electron currents are balanced with the electrons being retarded by the spacecraft potential relative to the space plasma and the ions being accelerated by it. Spacecraft charging is of concern because it can interfere with measurements made by scientific instruments that use the spacecraft frame as their reference voltage. More severe spacecraft charging can cause arc discharges to occur that damage electronics through electromagnetic interference. Dangerous levels of charging are predominantly a factor for spacecraft at geosynchronous altitudes and when lower altitude spacecraft pass through radiation belts and Auroral regions. Dangerous levels of spacecraft charging are generally not a concern for low Earth orbit spacecraft as ambient space plasma at these orbits is typically low energy and only capable of charging spacecraft to low voltages, less than one volt typically. An exception to this is when an active charged particle beam is emitted from the spacecraft, like an electron beam.

The emission of a high current electron beam (e-beam) from spacecraft in low to medium Earth orbit is a proposed experiment to probe the magnetic connectivity between magnetospheric and ionospheric phenomena [2]. High current e-beams require active mitigation of spacecraft charging as passive mitigation by collection of ambient space plasma electrons is insufficient causing the frame to float positive of the space plasma to an extent that electron beam emission is impeded. Active mitigation of spacecraft charging (both positive or negative) generally involves the emission of electrons or ions from the spacecraft using beam or plasma-based sources while passive mitigation uses a variety of methods such as field emission from surfaces and care to ensure that the entire spacecraft surface is conductive to prevent the creation of high electric fields between nearby surfaces (differential charging) [1].

The Beam-Spacecraft Plasma Interaction and Charging Experiment (B-SPICE), led by Gilchrist and Leon at the University of Michigan (UoM), was conducted to raise the technology readiness level of active mitigation of spacecraft charging during electron beam emission [3]. The sounding rocket experiment launched in November 2024, and UoM was assisted by Colorado State University's (CSU) Center for Electric Propulsion and Plasma Engineering (CEPPE) and the Los Alamos National Laboratory (LANL). The analysis of the flight data is currently ongoing. As part of B-SPICE, the CEPPE lab provided a plasma source instrument that mitigated e-beam caused spacecraft charging and thus enabled the emission of an electron beam on the sounding rocket. This thesis presents the development and characterization of the plasma source for the B-SPICE mission. A plasma source used to mitigate spacecraft charging is often referred to as a plasma contactor because it serves to 'short' the spacecraft to the local space plasma.

Section 1.2 - Plasma source review

There are many methods of generating plasma that were available for the B-SPICE mission. Two of which are briefly described below have historical applications in space as electric propulsion devices

for spacecraft, and the third being the source selected for the mission and the primary subject of this thesis.

1.2.1 - Gridded Ion Thruster

A Gridded Ion Thruster (GIT) operates using a plasma source that is placed in a positively biased enclosure that is open on one end. A set of gridded panels are placed over the open end that are biased such that the plasma source electrons are kept inside the enclosure while positive ions are accelerated out through grids allowing for the creation of an ion beam and the generation of thrust [4]. Equal numbers of electrons are provided to neutralize the ion beam by an externally located plasma electron source that transfers the electrons to the ion beam via a plasma bridge. The external plasma source is referred to as a plasma bridge neutralizer and the plasma it generates serves to both current and space charge neutralize the emitted ion beam. The generation of the internal and external plasmas used in a GIT can be performed using several methods such as DC, radio frequency, or microwave-based discharges. A GIT is designed so that ideally only ions pass through the grids and electrons in the beam plasma and neutralizer plasma bridge are prevented from backstreaming into the internal plasma region. The inclusion of the neutralizer external to the GIT to emit electrons into the ion beam is needed to prevent charging of the spacecraft. This aspect of the use of an ion beam generating GIT on a spacecraft is analogous to the use of a plasma contactor on a sounding rocket that emits an e-beam except that in the latter case the plasma contactor must emit ions at a rate that matches the rate of electron emission.

How could a GIT be adapted to serve as the active mitigation device for the BSPICE mission? First it is possible that an e-beam will assist in the current neutralization of the GIT ion beam, however it is not clear if the necessary space charge neutralization can be made to occur – without which the ion beam would not be able to be extracted. Consequently, while current neutralization might be facilitated by the electron beam in the B-SPICE mission, a GIT neutralizer might still be needed for space charge neutralization and for neutralization of ion emission current greater than the electron beam current.

A GIT adequate for the BSPICE mission would need to be about 20 cm in diameter and 20 cm long with a mass of about 5 kg. It would require three precision gas flow channels (two for the internal plasma and one for the external) and a gas storage system. A GIT also requires up to seven power supplies at a mass of about 10 kg to be started and operated, which along with the required size of the GIT and its complex expellant storage and feed system makes it an expensive, volumetrically large, high mass, and complex instrument for the active mitigation of charging of a high current e-beam sounding rocket mission.

1.2.2 - Hall Thruster

A Hall Thruster (HT) generates plasma within an electric and magnetic cross-field discharge region [4]. The electric field accelerates ions generating thrust while the magnetic field inhibits electrons emitted from the cathode from reaching the anode. The heating of the electrons in the ExB field region raises their temperature and energies to the point where they can generate the ions that are then accelerated from the HT into the plasma plume. These ions are neutralized by electrons emitted from a plasma bridge neutralizer that can be placed along the centerline of the HT or be mounted externally. Although the power supply set up for a HT is simpler compared to a GIT there are often at least five power supplies needed to start and operate a HT. A HT capable of neutralizing the BSPICE e-beam would need to be about 20 cm in diameter and about 15 cm long and would likely have a mass of close to 5 kg. Its power supply sub-system (~10 kg) and expellant storage and gas feed system would be similarly as complex as the GIT system.

A HT may be useful for neutralizing the electron beam emission on B-SPICE, as theoretically, if more ions are emitted by the HT compared to electrons by the e-beam then the self-neutralizing nature of the HT will keep the currents balanced. The feed system of the HT is also simpler than the GIT feed system as only two precision flow channels are required. Sounding rocket missions are relatively short, and we mention here that the time it takes to get a HT up and running would be very problematic for a short duration (7 min) sounding rocket mission. This same problem would apply to the GIT.

In our opinion, a plasma source that is simpler, smaller, less massive, and easier to start quickly and operate at high plasma production rates is needed

1.2.3 - Hidden Anode

The plasma source that has been chosen for B-SPICE is a device that is being referred to as the Hidden Anode Plasma Contactor (HAPC). It makes use of a hollow cathode like what a HT or GIT use for their neutralizers. The HAPC cathode is used to provide an electron current that is pulled toward an anode that is biased positive of the cathode. The anode is placed behind an orifice plate so that electrons are forced to flow through the orifice to reach the anode, this functions similarly to the remote arc plasma configuration described by Gorokhovsky (2012), Gorokhovsky (2017), and Gorokhovsky and Robertson (2018) [5] [6] [7]. This concept of having the cathode paired with an anode optically hidden from the cathode was also explored in the 1970's by Tisone and Bindell who used a similar hidden anode configuration for sputtering deposition purposes [8]. At the hidden anode orifice the incoming electron current meets a flow of outgoing neutral gas facilitating high collision rates due to high electron and neutral density and high electron energy. A wide range of ion-production currents can be reached by varying the flow rate of neutral gas and the current from the power supply biasing the anode. The HAPC, like a HT, benefits from self-neutralization of its plume while not needing the generation of a magnetic field, which accounts for most of the mass of the HT.

Section 1.3 - Hollow Cathodes

As stated before, the HAPC makes use of a hollow cathode similarly to what HTs and GITs use as their plasma bridge neutralizers. Hollow cathodes consist of a hollow tube with an orifice plate capping one end and a cylindrical insert placed in the tube and up against the orifice plate [4]. The insert acts as the electron emitter through thermionic emission that then ionizes neutral gas fed through the cathode creating a plasma that facilitates the movement of electrons from inside the cathode cavity out

through the cathode tube orifice. To assist in the initial operation of a cathode, a heater is sometimes used to preheat the insert to a temperature where thermionic emission can occur. Ion bombardment of the insert and subsequent recombination provides heating after ionization begins allowing the heater to be turned off during continuous operation. A keeper is additionally paired with a cathode to facilitate the initial starting of the cathode, maintain operation during interruptions, and protect the cathode from high-energy ion bombardment. The HAPC makes use of a hollow cathode that doesn't use a heater. Using high mass flow rate for a heaterless cathode allows repeatable instant starting [9]. This instant start is why this type of cathode was selected for the restricted time of a sounding rocket mission. The specific cathode used in this thesis was donated by Plasma Controls LLC [10]. The insert for the hollow cathode is a ceramic-metal based material containing tungsten, nickel, and barium-calcium-aluminate with scandate [11].

Section 1.4 - Thesis Structure

Concluding this introduction, the remainder of this thesis will follow with a description of the hardware and performance requirements of the HAPC to support the B-SPICE mission. This will be followed by a description of the testing apparatus and procedures used to characterize the HAPC ion production rates and determine the shape of the expanding plasma plume along with the plasma properties of plume and the ion energy and charge state distributions. Next, we report and discuss the results of the testing campaign, and then we end with our concluding remarks and recommendations on future work. Although the hardware development and determination of operational conditions of the HAPC that support the B-SPICE mission are the primary desired outcomes of our efforts, of equal or greater importance is the characterization of the plasma emitted by the HAPC, as these data will be used by modelers as inputs to their simulations to study the electron beam propagation from a sounding rocket while an active charge mitigation system is being operated.

Chapter 2 - B-SPICE Elements

In this chapter we briefly describe the B-SPICE sounding rocket experiment and the requirements it imposes on the HAPC. Next, we discuss the gas flow storage and control sub-system, the hidden anode and hollow cathode elements, and the electronic control sub-system of the HAPC instrument.

Section 2.1 - B-SPICE HAPC Performance Requirements

The B-SPICE e-beam is set to run at 200 mA of emitted electrons for the mission. The focus of the flight experiment is the first of two sequences of operation of the e-beam and HAPC with a period of just the e-beam, a period of just the HAPC, and then both together. The mission had a short, seven-minutes-long duration available to perform the science limited by the sounding rocket flight time. With this time restriction the HAPC needs to turn 'on' quickly. When the HAPC is operated alone, three 'on' periods were tested of 50 ms, 200 ms, and 400 ms with this period allowing the plasma plume to expand before the e-beam is turned on to accompany the HAPC. The HAPC was also operated at 5 different ion production currents in the first science sequence. Targeted ion production currents are 100 mA, 150 mA, 200 mA, 250 mA, and 300 mA. Science sequence 1 (SSQ1) also has the HAPC running at a 10% expellant utilization efficiency. Utilization efficiency is the ratio of ion production current to the gas flow rate measured in ampere equivalent (Aeq), with the parameter used to indicate how much of the neutral gas flow is converted to ions accelerated from the HA. To achieve higher ion production currents at constant utilization efficiency the HA needs an increase in current sent to the HA and an increase in flow rate, with higher utilizations requiring even higher inputs of current.

The second science sequence (SSQ2) doesn't vary the time the HAPC is 'on' without the e-beam being 'on', but instead tests two additional utilizations, 20% and 30%. SSQ2 also only operates at 200 mA, 250 mA, and 300 mA ion production current levels. To control both ion production currents and the

utilization for the science sequencing, the voltage and current supplied to the HA need to be controlled along with the flow of krypton gas.

As explained in Section 1.4, an additional part of B-SPICE is a computer simulation activity to predict the behavior of the rocket charging and gain a better understanding of the physics behind this process while an active charging mitigation system was being operated. An experimental characterization of the HAPC in each operational state is needed to provide input data for the simulation to use to calculate the evolution of the HAPC plume before the e-beam was turned 'on'.

Section 2.2 - Flow control/controller

A flow control system was needed to feed krypton to the HAPC. The chosen system was developed in-house at the CEPPE lab using a combination of custom designed and COTS parts. The flow control system can provide krypton flow to both the cathode and anode from a gas storage tank using solenoid valves (to both initiate flow and for complete flow shut off), proportional flow control valves (pfcs), and precision orifices. Figure 2.2-1 below shows the general layout of the flow system. A manual valve is used to fill the 300 mL volume storage tank prior to testing and flight.

The operation of the flow control is based on the choked-flow as expressed by Equation 2.2-1, which uses the orifice size, the stagnation pressure upstream of the orifice, the orifice temperature, and gas properties of Kr to predict the flow rate.

$$\dot{m} = P_0 A^* \sqrt{\frac{k}{RT}} \left(\frac{2}{k+1}\right)^{k+1/2(k-1)}$$

Equation 2.2-1

In Equation 2.2-1 $\dot{m}$ is the mass flow in kg/s, P^* is the stagnation pressure in Pa, A^* is the orifice area in m^2, k is the ratio of specific heats, R is the specific gas constant in J/(kg*K), and T is the gas temperature in Kelvin.

The flow system has krypton gas stored in the tank that is passed through a solenoid valve to a manifold that has the pfcs and pressure transducers (PT) mounted to it and then through this manifold to a line leading to the cathode or anode. In either line, the gas then flows through a precision orifice where choked flow is assumed to occur. The PT in each line is used to measure the gas stagnation pressure. After flowing through the orifice, the gas then flows through another solenoid valve that allows total flow shut off for each line to be achieved independently. With the selected solenoid valve open, the gas flow then continues to either the cathode or anode as desired. The thicker lines with arrows in Figure 2.2-1 are the gas flow paths while the less thick lines indicate the telemetry or control lines. The orifices that are located just downstream of the PTs are not shown in the diagram.

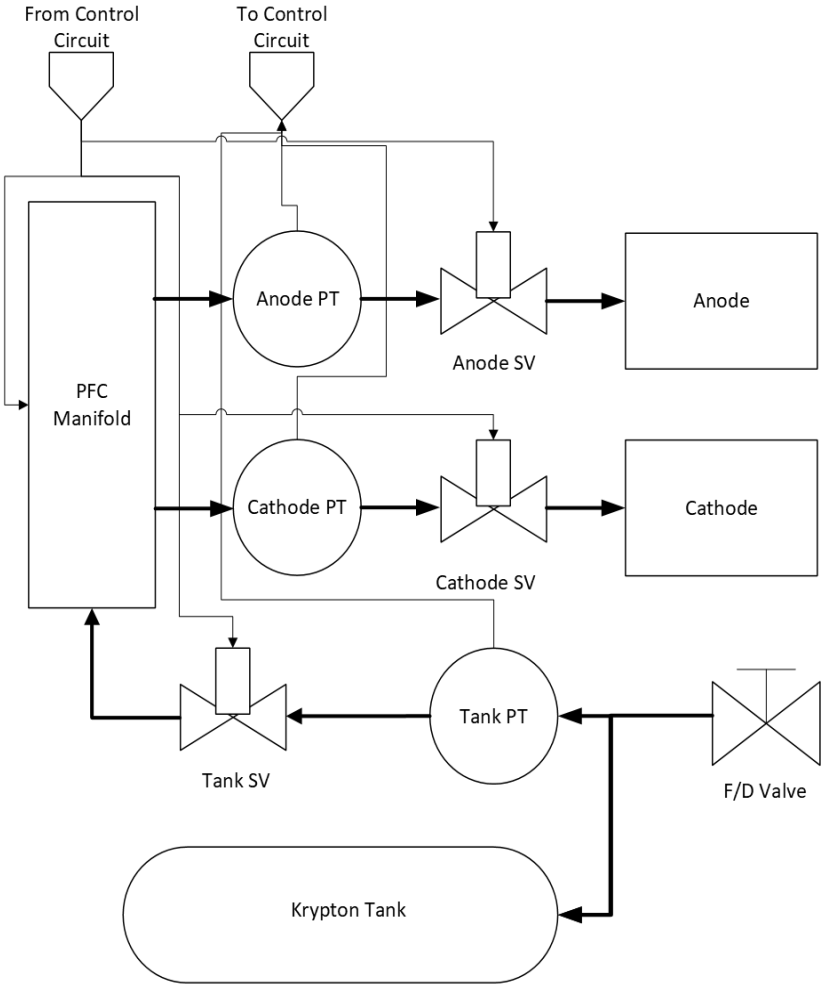

Figure 2.2-1: HAPC Krypton Feed System

For control, the signals proportional to the stagnation pressures are input to a printed circuit board that has analog proportional-integral-derivative (PID) configured controllers that take the PT signals and compare them against set point signals known to set a specific flow. The PID circuits then adjust the supplied current to the pfcs changing how much they are actuated. This in turn adjusts the stagnation pressures and the PTs send new signals to the PID, which continues to adjust the current to the pfcs until the differences between the pressure signals and set points are zero. Figure 2.2-2 is a circuit diagram of one of the PID controller circuits on the pcb. The PID circuit was designed in coordination with Dr. Cody Farnell. The feed system was shown to be able to set the flow rate to a desired value in less than 100 ms.

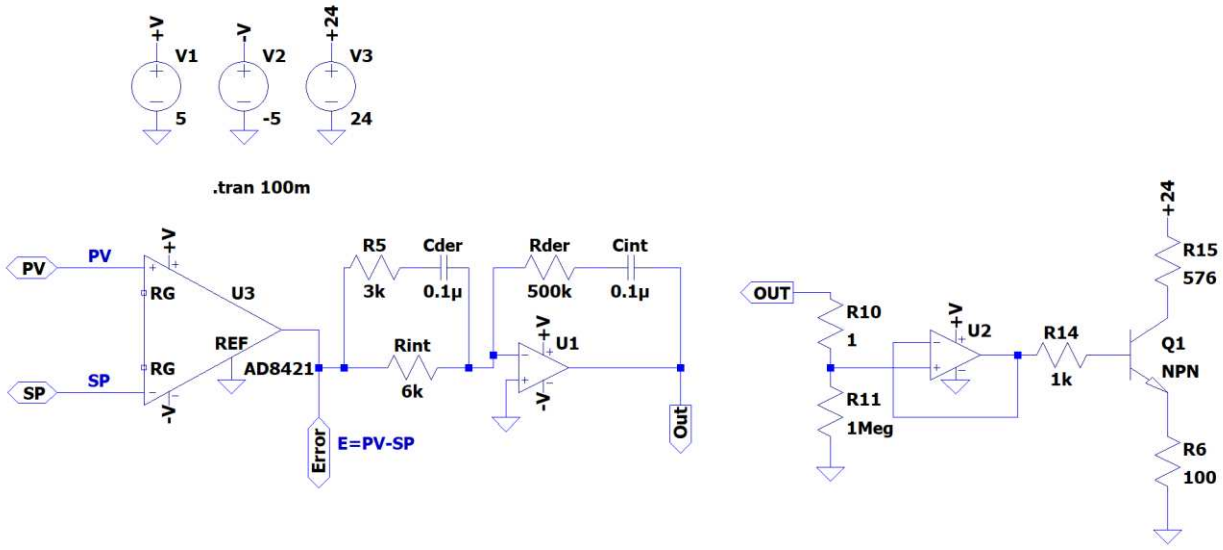

Figure 2.2-2: Circuit Diagram of PID Controller

Section 2.3 - Hidden anode and hollow cathode

The Hidden Anode Hollow Cathode (HAHC) assembly is the plasma source in the HAPC system. As described earlier it functions with the cathode providing an electron current that flows through the anode orifice. The orifice is a bottleneck location for the electrons and the neutrals that counterflow against one another there. This location and regions nearby are where the electrons produce ions. Prior to start up, the keeper electrode for the cathode is biased to 500 V positive of the cathode with a DC power supply. To start the cathode a flow of 100 sccm of krypton is provided that is reduced to 10 sccm after

the cathode-keeper plasma discharge is ignited. Anode operation is initiated after cathode ignition by flowing krypton gas through the anode at flows between 4-31 sccm. The anode is biased positive of the cathode by a DC power supply to 250 V with the supplied current varying from 0.4-2 A depending upon the operational state desired. The anode orifice plate "hiding" the anode is likewise biased positive of cathode with the same power supply as the anode but with a 150 kOhm resistor in-line to limit the allowed current that can flow to the anode orifice plate. Figure 2.3-1 shows a diagram of the electrical circuit. The blue hemispherical region shown downstream of the hidden anode is where intense plasma generation occurs with the highest ion production rates occurring close to and possibly within the anode orifice.

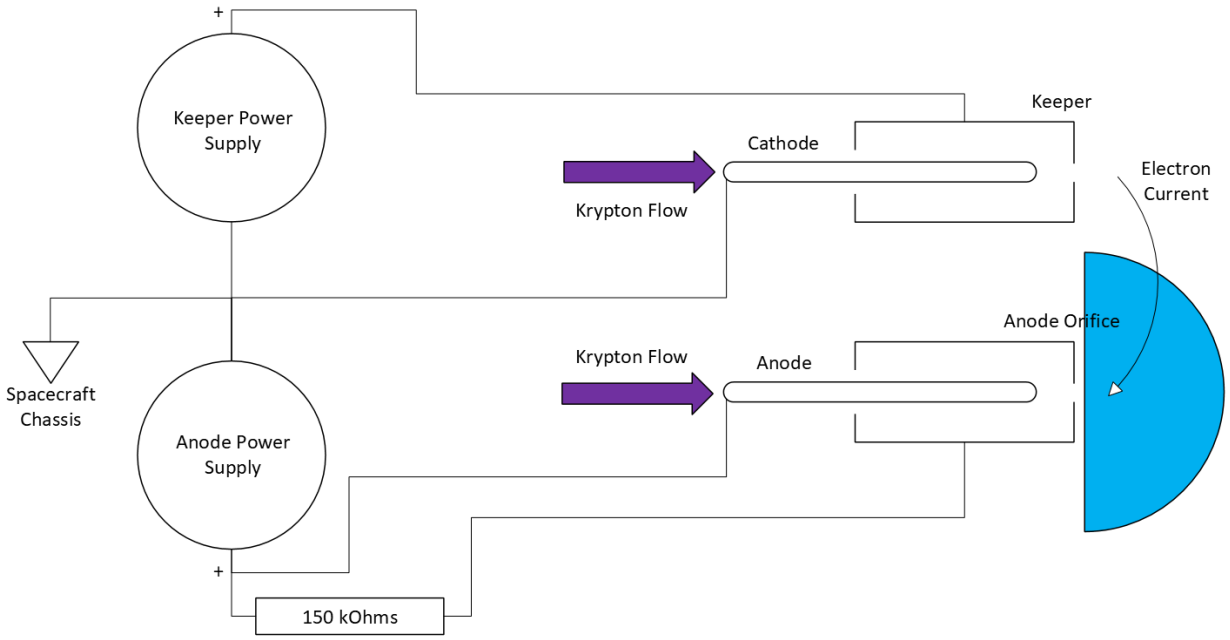

Figure 2.3-1: HAPC Circuit Diagram

For B-SPICE the cathode is tied through a current sensor to the rocket chassis to allow current to the rocket body to be monitored. The hidden anode uses an identical hardware configuration to the hollow cathode and keeper pair except for the exclusion of the ceramic-metal insert.

Section 2.4 - Electronics sub-system

The flow control circuit previously described in Section 2.2 and the power supplies needed for the HAPC operation described in Section 2.3 are housed in an aluminum box that also houses the DC-DC conversion board, a voltage and current monitoring board, and a board with a microcomputer that is the controller of the entire HAPC system. The DC-DC board takes the battery power supplied by the rocket and outputs DC voltages needed for operation of the other boards and power supplies. The microcomputer board takes the measured data values of the voltage, current, and pressure transducers in the HAPC and passes the data on the main computer of the B-SPICE payload, which records and stores that data for later analysis. The HAPC's computer also takes commands issued by the main computer about what state the HAPC should be in and then the HAPC microcontroller sets all operating conditions to the corresponding state while communicating the state of the HAPC back to the main computer. The voltage and current monitoring board uses voltmeters and hall sensors to measure the voltages and currents for the anode, anode orifice, and keeper as well as the current from the cathode to the rocket chassis. This electronic box and the boards used were designed by Dr. Cody Farnell as part of the HAPC project for B-SPICE. Programing of the microcomputer and an interface program run on a standard computer for testing and issuing commands to the HAPC microcomputer was done by Dr. Shawn Farnell. Figure 2.4-1 contains a photograph of the HAPC being set up for testing in a CEPPE vacuum chamber.

Figure 2.4-1: Photograph of HAPC Hardware Set Up for Testing.

Chapter 3 - Apparatus and Procedures

In this chapter we discuss our testing apparatus and procedures for characterizing the HAPC in support of B-SPICE. The first section goes over the power supplies, diagnostics tools, and HAPC control electronics used during testing. Following that is a description of the vacuum chamber that was used for testing the HAPC. The remaining sections cover the probes utilized to perform plasma property measurements.

Section 3.1 - Setup

The HAPC hardware that was tested in this thesis was the back-up flight hardware unit for the B-SPICE experiment. The plasma diagnostics tools described below used Electrometer/Sourcemeter/ Multimeter systems for data acquisition and probe operation. Spare circuit boards of the flow control, microcomputer, and Voltage/Current monitoring boards were used to run the HAPC hardware during plasma diagnostic testing to match flight hardware as much as possible. Power supplies for the Keeper and Anode were lab rack supplies manufactured by TDK Lambda that mimicked the flight hardware power supplies. Specifically, a TDK Lambda model GENH600-1.3 was used for the keeper and a GH600-2.6 was used for the anode. The anode power supply used an analog control scheme allowing the microcomputer board to control the current setting of the PS allowing the HAPC interface program to be used in controlling the HAPC and data logging the pressure, voltage, and current transducer measurements. The HAPC power supply positive outputs were connected to diodes and ballast resistors and flyback diode circuits were used across the power supplies to protect them and the HAPC from power surges or unstable HA operation. Figure 3.2-1 is a photo of the server rack which held the electronics used for running the HAPC.

Section 3.2 - Testing Facilities

Plasma diagnostic testing of the HAPC was done in the Orion vacuum chamber in the CEPPE laboratory. The cylindrical chamber is 1.7 m in diameter and 4.6 m in length. High vac pumping was handled by two Varian HS20 diffusion pumps backed by a Leybold DryVac rough pump. The two diffusion pumps allowed base pressures of 7e-6 Torr to be achieved with a pumping speed of 10,000 L/s pumping Krypton. This set the chamber pressures during HAPC operation at ~2.4e-5 Torr with just the cathode running to ~11.4e-5 Torr at highest Anode flow state. Figure 3.2-2 below provides a diagram of the test chamber.

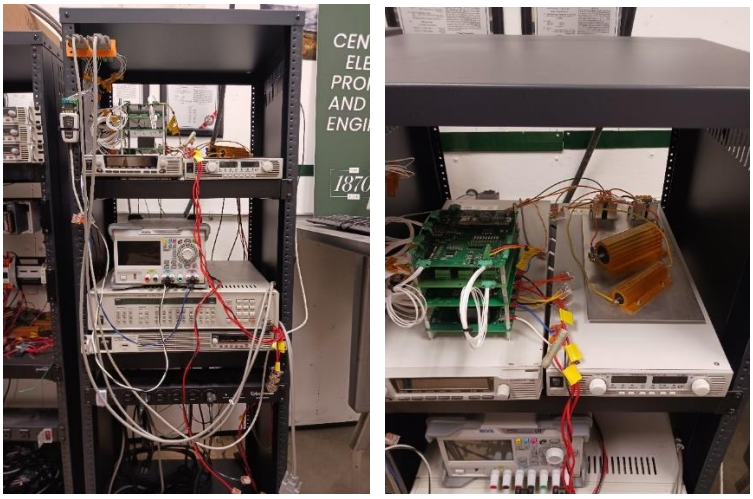

Figure 3.2-1: Photographs of Rack Holding PCBs, Power Supplies, and Protection Electronics.

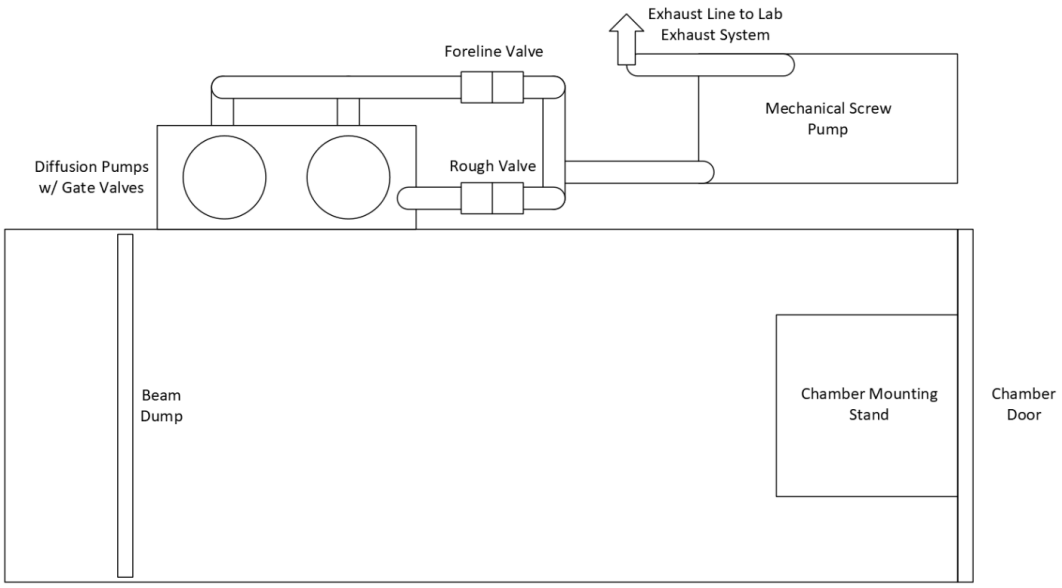

Figure 3.2-2: Vacuum Chamber Layout

Section 3.3 - Probes

Plasma diagnostics were done using a magnetically shielded current density (CD) probe, a Langmuir probe (LP), a retarding potential analyzer (RPA), an ExB probe, and an electrostatic analyzer (ESA) that has the addition of another ExB probe in line with the ESA's exit, the combination of which is referred to as an E-VADER. All of the above probes were manufactured by Plasma Controls, LLC and loaned out to CSU for the testing described herein. The CD probe was mounted on a single rotary motion arm with the center of rotation aligned with the anode orifice so that it moved on a hemispherical arc with the anode orifice at the origin. All other probes were mounted to another motion stage with 4 axes of motion. The axes are indicated in Figure 3.3-1, with *Z* along the length of the chamber, *R* the width, *Y* the vertical, and *T* a rotational axis allowing the probe mount to be angled in relation to the test stand with the HAPC. The Primary use of the 4-axis motion stage was for probe alignment and centerline distance variation. Each probe could be moved to match the centerline alignment of the anode orifice.

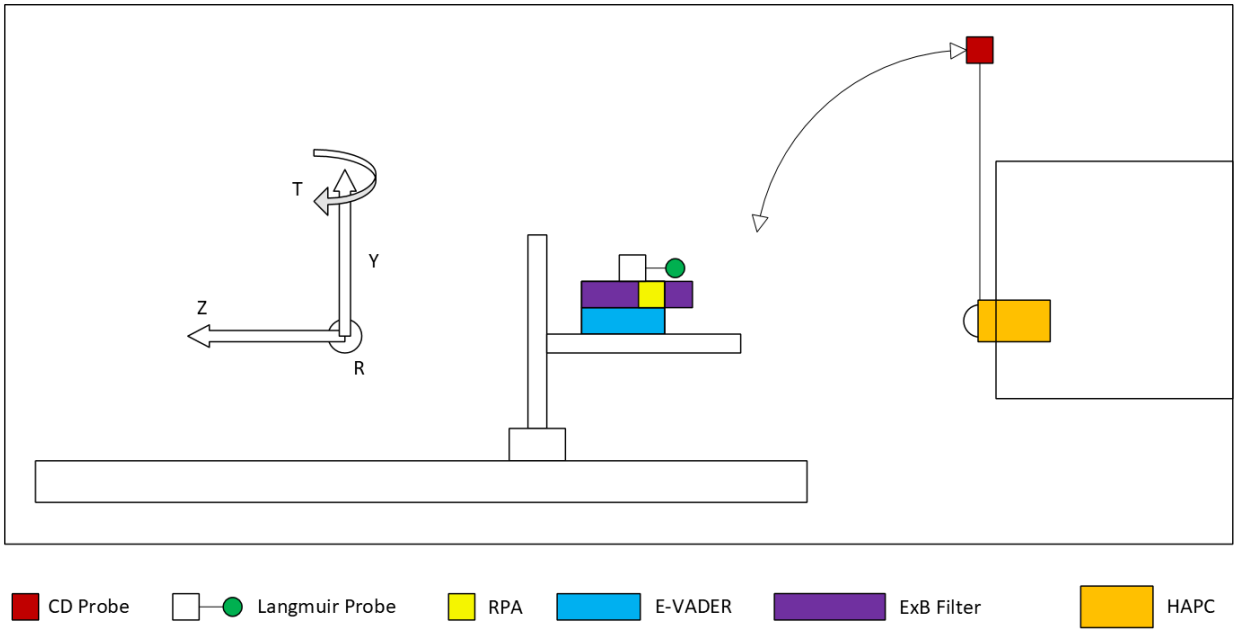

Figure 3.3-1: Probe Positions in the Vacuum Chamber.

3.3.1 -Chamber Biasing and Faraday Probe

Two techniques were used to evaluate the ion current produced by the HAPC. The first technique involved pulse biasing the HAPC relative to the vacuum chamber walls. The second technique was to use the CD probe to measure the profile of the emitted ion current density and then integrate this profile. Pulse biasing the HAPC was performed using a Keightley 2601 sourcemeter to bias the HAPC positive relative to the chamber to attract ions to the chamber walls while repelling electrons. The current recorded by the sourcemeter as a function of the pulse bias magnitude was recorded, and at sufficiently high biases, the current was observed to saturate. This current was taken to be the ion production current produced by the HAPC that expands from the source to regions downstream. The biasing is pulsed so as to limit the capacitive impedance of contamination on the chamber walls [12]. Pulsing the bias at a fast rise time reduces the effects of wall contamination by shorting through the contamination layer capacitance. The measured current was recorded after the displacement current signal had dissipated and then was corrected for ion induced secondary electron emission. We believe that this measurement technique overcomes the complications caused by charge exchange reactions that plague other ion production

measurement schemes. We also judge that ion recombination rates from two and three body processes are negligible at the densities and electron temperatures in the HAPC plume.

The CD was used to measure the ion current density profile of the HAPC that would be representative of the shape of the plasma expansion from the source [13]. This current density profile can also be used for calculating ion production rates by integrating it over a hemisphere with a radius defined by the probe motion. The CD probe used consisted of a graphite collector plate and guard ring and was magnetically shielded to suppress collection of electrons. The collector and guard ring were biased 20 volts negative of the chamber walls by a dc power supply with the current to the collector plate determined from the voltage drop measured across a 1-kohm resistor. This voltage drop was read by an Agilent 34401A 6 ½ digital multimeter. The CD probe was swept across a 150° vertical arc in front of the HA with the coordinate zero positioned on the center line of the HA. Two or more sweeps were made for all operational states except for the states at 200 mA and 250 mA with 30% expellant utilization due to the erosion of the anode orifice diameter that was observed at these operating conditions. All sweeps for the 10% utilization target states had the current density measured in 2° intervals with the probe being moved to and then held at each interval while the HAPC was operated continuously. The 20% and 30% target utilization sweeps used step sizes of 10° to minimize the run time of the HAPC at these conditions.

3.3.2 - Langmuir probe

A LP was used for measurement of plasma potential, floating potential, electron temperature, and electron density in the plasma plume. LP traces were taken at three different distances from the HA, all along the centerline, to characterize variation with distance in each parameter. The LP functions to collect a current from the plasma plume when biased, with the specific voltage bias influencing the number of ions versus electrons collected and this in turn determines whether the net current to the probe is positive or negative [14]. When the net current is equal to zero (ion and electron currents are equal) the probe is said to be at the ‘floating’ potential, which typically occurs at a potential negative of plasma

potential that is about 4-5 times the electron temperature (measured in eV) of the plasma. The reader is referred to Chen for more details on LPs [15].

The LP used herein consisted of a 1.25" diameter stainless steel sphere with a ceramic insulator to electrically isolate it. Electrical connection is done through a single wire that passes into BNC triaxial cables and chamber feedthrough that led to the Keithley 2601 sourcemeter used to bias the probe. The probe was pulse biased to mitigate the effects of contamination on the probe surface to the current measurements [16]. The LP voltage was scanned from -15V to 25V with the pulse 'on' and 'off' time both being 0.01 seconds. The scanned voltage range was divided into 141 discrete test voltages.

3.3.3 - RPA

An RPA was used for making ion energy distribution function measurements, and the interested reader is referred to the reviews by Ferda and Lai and Miller to learn more. [17]- [18]. We used a four-screen-with-collector design to reduce the effects of ion induced secondary electrons on the measurement. The collector plate current was read with a Keithley 6517B Electrometer/High Resistance Meter while grid biasing used a Rigol DP932A 3-channel power supply. The collector plate was 0.5" diameter 316 stainless steel disc and was behind four 316 stainless steel grids with a total transmission of ~35%. The RPA model was designed and constructed by Plasma Controls LLC. A graphite body housed the collector plate and four grids. An RPA functions by biasing grids in front of a collector plate and selectively filtering out ions by sweeping the potential of one of the grids over a range of values that only allows ions with kinetic energy higher than this potential to pass through to the collector. In our four-grid configuration, from outermost to innermost, the first grid is grounded or floats and reduces plasma disturbances, the second is biased negative and repels electrons. The third grid is swept over a range of biases to reject ions of increasing energy, and the fourth suppresses secondary electron emission from the collector. The collector then measures the current of received ions as a function of the voltage applied to the third grid.

3.3.4 - Electrostatic Analyzer and Wein Filter

In addition to the RPA, an Electrostatic Analyzer (ESA) was used to measure the ion energy distribution. This was done to confirm the distribution across both probes. The ESA works by deflecting ions with specific energy-charge ratios (E/q) through a curved optic path with the accepted E/q determined by the voltage difference between two curved plates creating the optic path and deflection force with the produced E-field or through varying an acceleration/deceleration voltage at the entrance [19]. The specific ESA used in testing was part of a combination probe developed by researchers at CSU as described by Thompson, Seth J., et al, and so has a Wein filter in line with the ESA with the combination referred to as the Energy and Velocity Analyzer for Distributions of Electric Rockets, or E-VADER. A top view of the E-VADER is in Figure 3.3-2. The E-VADER can also be configured to run exclusively the ESA and so can take standard ESA measurements, and this was done for the testing described herein.

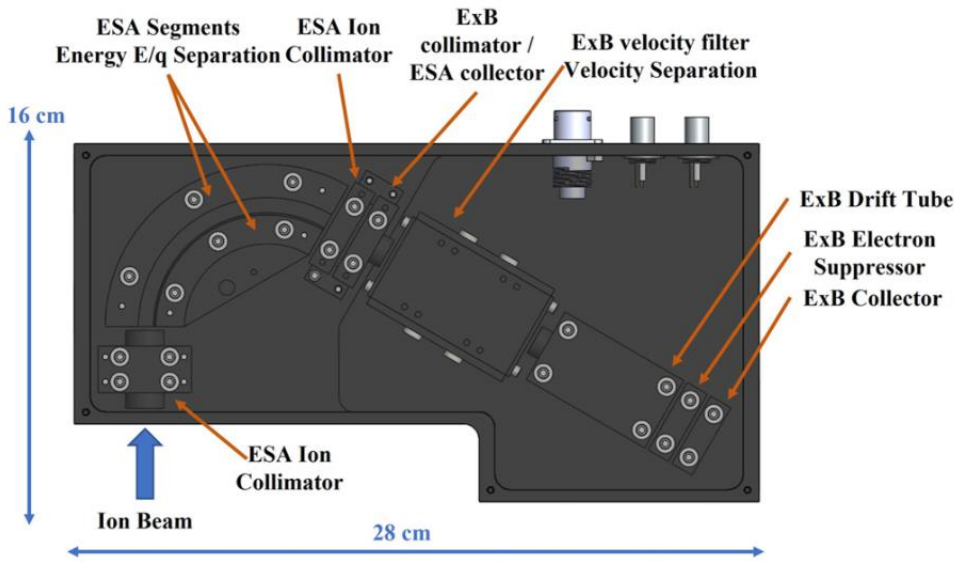

Figure 3.3-2: Figure Taken from "Combined electrostatic analyzer—Wien filter probe for characterization of species distributions in hall thrusters."

A Wein velocity filter, or ExB probe, was used to determine the charge state fractions of the ion population [20]. Electric and magnetic fields normal to the path of ions and to each other are used to deflect ions off the path depending on the velocity of the ion. If an ion passing through the filter has a

velocity that balances the forces from the E and B fields, satisfies $\vec{E} = -\vec{v} \times \vec{B}$, then the ion is accepted and passes to a collector electrode at the end of the probe. A scan of ions with different velocity is achieved by holding the magnetic field held constant and sweeping the e-field is swept by varying the bias applied between two parallel plates. This scan can be used to create a current-vs-voltage plot with peak structures that can be used to extract relative charge state concentrations. From the collected data, integration of curves fitted to the peaks was used to determine charge state fractions.

As stated, the E-VADER combines an ESA with an ExB probe such that ions pass through the ESA and filtered based on their E/q with accepted ions passed along to the ExB probe [19]. With this technique one avoids the common problem encountered with plasma sources that create ions with wide spreads in energy of ExB spectra that have overlapping charge state signals. The better resolved ExB spectra taken across multiple energies vastly simplifies the analysis of ExB probe data allowing for more accurate analysis of charge state fractions. However, while this configuration can provide easier to interpret data, the process can be slow and requires multiple scans to get a full picture of the ion characteristics. The slow data collection process can extend over tens of minutes and can be of concern for certain operational states of the HAPC as erosion of the orifice in the HA was observed in testing and occurs at rates that makes prolonged testing at these states unfavorable. A stand-alone ExB probe was used to collect charge state data for these HAPC operational states, which were for the 20% and 30% target expellant utilization efficiencies desired in the second science test sequence of the BSPICE mission. All 10% utilization efficiency operational points were able to make use of the ExB probe in the E-VADER as anode erosion was found to not be a concern for these conditions.

Both the ExB and ESA sections of the E-VADER, and the standalone ExB used a Keithley 6517B Electrometer/High Resistance Meter. The ESA had a mean optic path radius of 5 cm over a 120° long arc. Both entrance and exit collimators have 0.152 cm orifices, the entrance having two orifices separated by 3.2 cm giving a ±2.75° acceptance angle at the entrance. The E-VADER and ExB probe were mounted to the motion stage as described earlier in this chapter.

Chapter 4 - Results and Discussion

The following sections contain details related to the experiments that were performed on the HAPC needed for understanding the physics behind B-SPICE experimental data. First we describe the shape of the plasma plume that expands downstream of the HAPC. This section is followed by a discussion of ion production current measurements and characterizations of the electron and ion properties of the plasma plume. Finally we conclude this section with a discussion of the erosion of the hidden anode orifice under different operational conditions of the HAPC.

Section 4.1 - Plasma Plume Shape

One process for measuring ion production currents involved taking measurements of current density along a hemispherical arc centered on the HA orifice as described in Ch. 3. As the CD probe can only move along a single axis over an angular range of about 150° and the HAPC had mounting restrictions, the CD data was split into two sections—one above the centerline of the HA and one below. Curves fits were made to these data by folding them to put all angular positional data between 0° and 90°. The ion production current would then be the result of a double integration, integrating the fitted curve over the area of a full hemisphere assuming azimuthal symmetry. The underlying assumption of azimuthal symmetry for the CD traces was judged to be qualitatively not very good however and the other method, described in Ch 2 and in Section 4.2 below, was used to find the ion production current, which we believe is more accurate. The CD data are still useful as they can be used to describe the shape of the plasma expanding from the HAPC.

Data from CD probe sweeps are processed for corrections from effects like low energy ion induced secondary electron emission (IISEE). Corrections for attenuation of the high energy ions leaving the HA via charge exchange were also made using Equation 4.1-1, where the current density is j, the corrected current density is j_{corr}, n is the number density of neutrals in the chamber in the region between

the HA and the CD probe, σ is the charge exchange cross section of krypton found using Equation 4.1-2 [21], with E the energy of the ions in eV taken as the most probable ion energy from the IEDF data collected with the RPA and ESA diagnostic tools, and r is the probe distance from the HA, which was set at 71 cm.

$$j_{corr} = \frac{j}{\exp(-n\sigma r)}$$

Equation 4.1-1

$$\sigma = 80.7 - 14.7\log(E) * 10^{-20}$$

Equation 4.1-2

Ion induced secondary electron emission is the phenomena were by the impact of an ion on a surface can emit an electron from the surface, which can then be accelerated away from a negatively biased surface of a probe and affect the measured current by inadvertently counting the ion twice [13]. Corrections for IISEE and the physical gap between the collector and guard ring on the probe are needed to perform this correction. The ion current density, j, is calculated from the collected ion current, I_{FP}, the area of the collector, A_C, the gap correction figure, K_G, and the SEE correction factor, K_{SEE}, with Equation 4.1-3 providing this calculation.

$$j = \frac{I_{FP}}{A_C + K_G} K_{SEE}$$

Equation 4.1-3

K_G is derived from the geometry of the probe, using the inner radius of the guard ring, R_{GR}, the radius of the collector, R_C, and their respective heights, h_{GR} and h_C, where Equation 4.1-4 is the formula for K_G.

$$K_G = \pi(R_{GR}^2 - R_C^2)\left(\frac{2\pi R_C h_C}{2\pi R_C h_C + 2\pi R_{GR} h_{GR}}\right)$$

Equation 4.1-4

The parameter K_{SEE} is calculated using Equation 4.1-5, using the IISEE yield of the kth species, γ_k, the kth ion species current fractions, Ω_k, and the ion charge state Z_k.

$$K_{SEE} = \frac{1}{1 - \sum_k \frac{\Omega_k \gamma_k}{Z_k}}$$

Equation 4.1-5

The IISEE yields are dependent on the material of the surface struck by an ion in addition to the type of ion [22]. The CD probe is made from graphite, which has an IISEE yield of 0.04 for Xe ions and 0.2 for Ar ions (singly charged) at ion energies less than 500 eV. The IISEE yields for graphite were unavailable for Kr ions, and so we assumed an IISEE yield of 0.1 for singly charged ions. Doubly charged ions generate more secondary electrons, and we used a similar approach to come up with an assumption of an IISEE yield of 0.3 for Kr doubly charged ions [23]. As graphite and tungsten have similar work functions, 4.38 - 5.0 eV and 4.2 - 5.99 eV, respectively, IISEE yields for tungsten on krypton can also be used as an estimate for graphite. The yields for Kr ions on W are 0.05, 0.3, and 0.85 for singles, doubles, and triples, respectively [24] [25].

All current density sweeps indicated a nearly diffuse distribution of ion emission from the HA. Current densities fluctuate some with respect to angular position but largely held consistently for a single state except for one area of the arc. When the CD probe was at angular positions that had the hollow cathode partially between the probe and the HA an attenuation of the measured current occurred for all states. There is no physical blocking of current occurring at these angles, unlike the full 90° off normal position which has the CD probe hidden from the HA by the mounting stand of the chamber, so what is attenuating the current measured here is unclear. A possibility is the neutrals emitted by the cathode attenuates some of the ions from the HA through charge exchange collisions and this suppresses the current density measured in the regions of the CD probe arc nearer to the cathode. Figure 4.1-1 below shows a polar plot of CD measurements with a diagram of the HAPC to illustrate the plume shape.

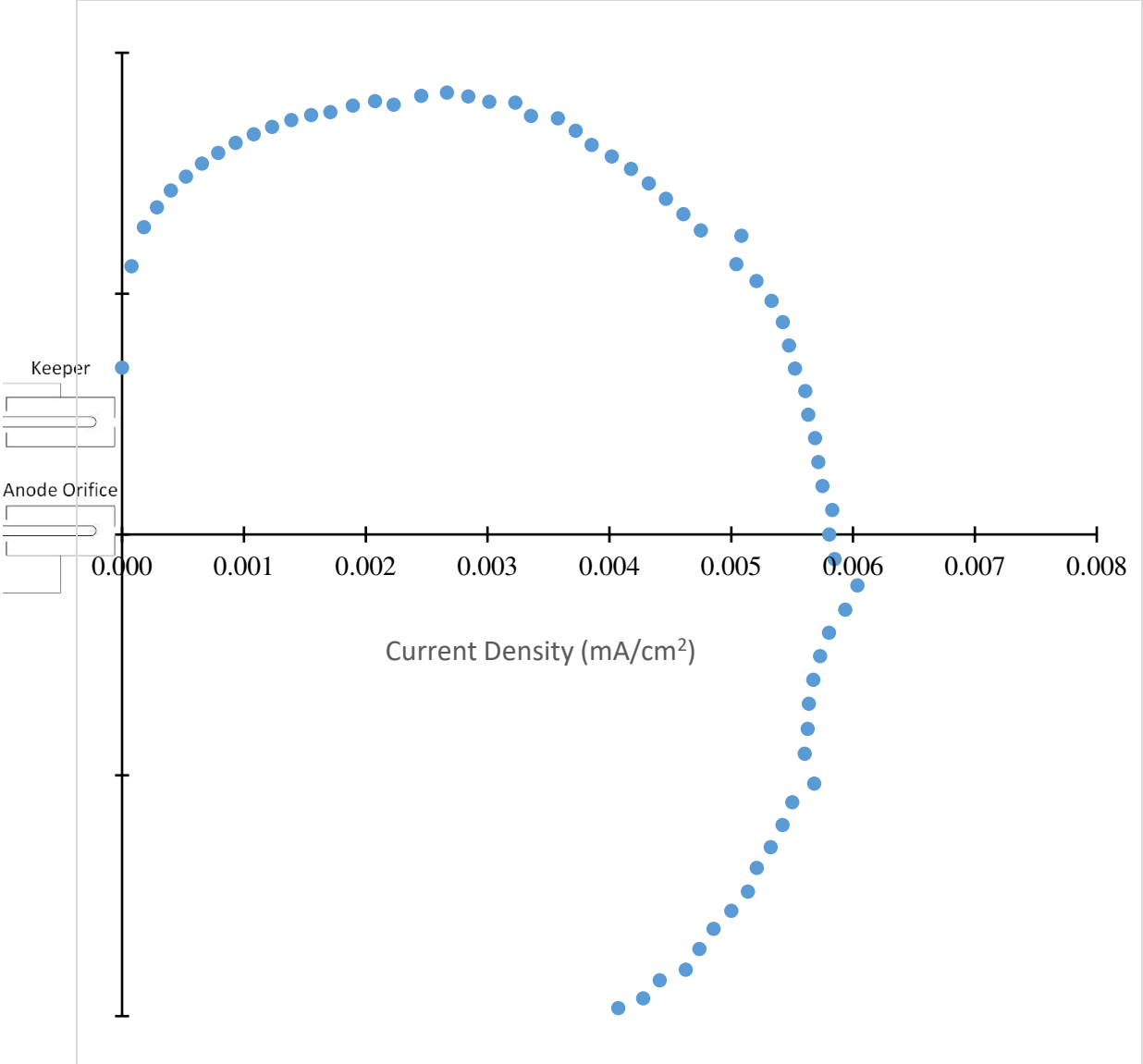

Figure 4.1-1: Plasma Plume Shape Plot from CD Measurements.

The asymmetry of the plasma plume is made more evident when the data points are folded to be in one quadrant, as shown in Figure 4.1-2. Here we see how the section of the CD data taken at angular positions opposite the cathode has greater current densities. Also plotted are a uniform hemispherical distribution (point source diffuse expansion), a cosine distribution (planar diffuse point source expansion), and the polynomial fit distribution used in the integration technique discussed in Section 4.2 below for finding the total ion production current from CD data.

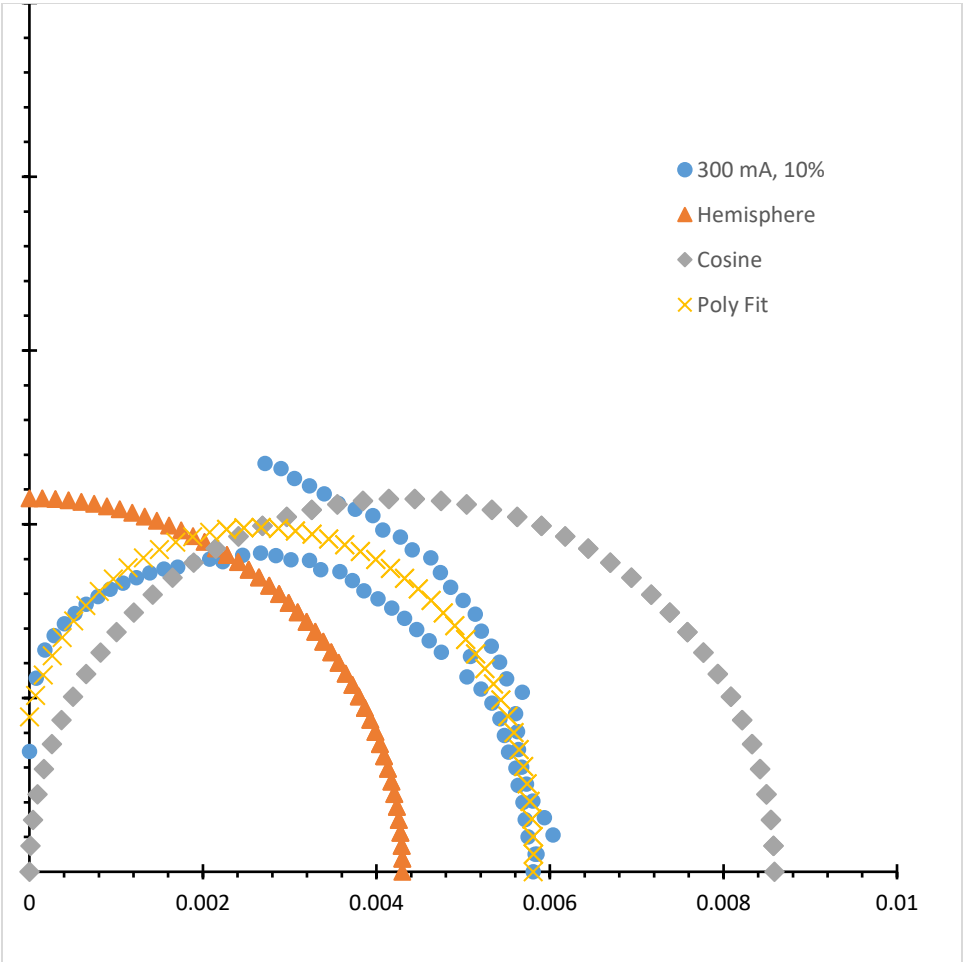

Figure 4.1-2: CD Trace for 300 mA at 10% Utilization with Data Folded to be in One Quadrant. Includes an Ideal Quarter Circle Trace for Comparison

The distortion of the plume from being a full hemisphere is likely due to the geometry of the HA itself and that most of the ion production is occurring very close to the HA orifice plate. The anode orifice plate that hides the anode and restricts the electron flow is held on by a molybdenum nut. This nut encircles the orifice plate and juts out further than the plane of the orifice plate. This likely causes a surface where expanding ions created close to the orifice can impinge upon and be removed from the expanding plume. As mentioned above, the expansion nearly follows a cosine expansion, but with reduced flux along the centerline relative to a cosine distribution and enhanced flux at larger zenith angles, which is often referred to as an under-cosine distribution. The under-cosine distribution falls between the cosine and full hemispherical distribution shapes suggesting that the ions are not emitted

from a true point source as a hemispherical distribution would indicate nor from a planar point source as a cosine distribution would indicate. Figure 4.1-3a shows a photograph of the HA with the anode orifice and mounting nut while Figure 4.1-3b shows a section view of the CAD for the HA assembly. The under-cosine distribution suggests the ion production processes happening near the HA orifice are distributed over a small region within the orifice and slightly downstream of the orifice, and this distributed region of ion production is what results in the shape of the expanding plasma.

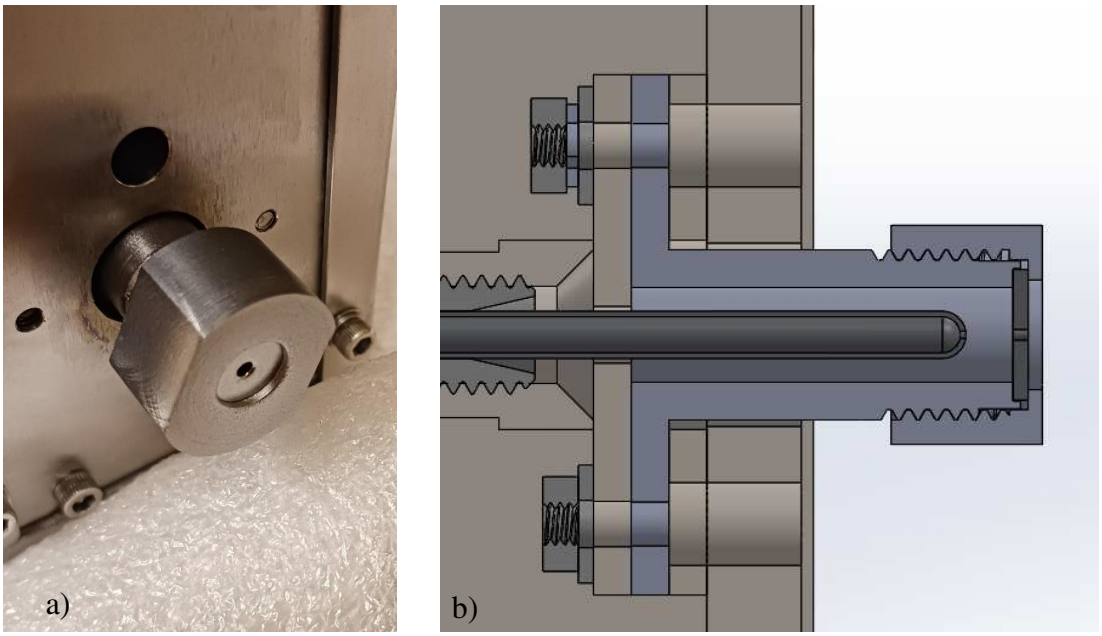

Figure 4.1-3: a) Photograph of the HA assembly. b) Section view of HA CAD

The under-cosine plume shape is consistent across all science sequence operational states. Only the current density magnitudes vary between each state, which is expected due to variation in the achieved ion production currents. Figure 4.1-4 shows the CD profiles for the 300 mA and 200 mA states at 10% expellant utilization efficiency along with the 300 mA and 20% utilization data.

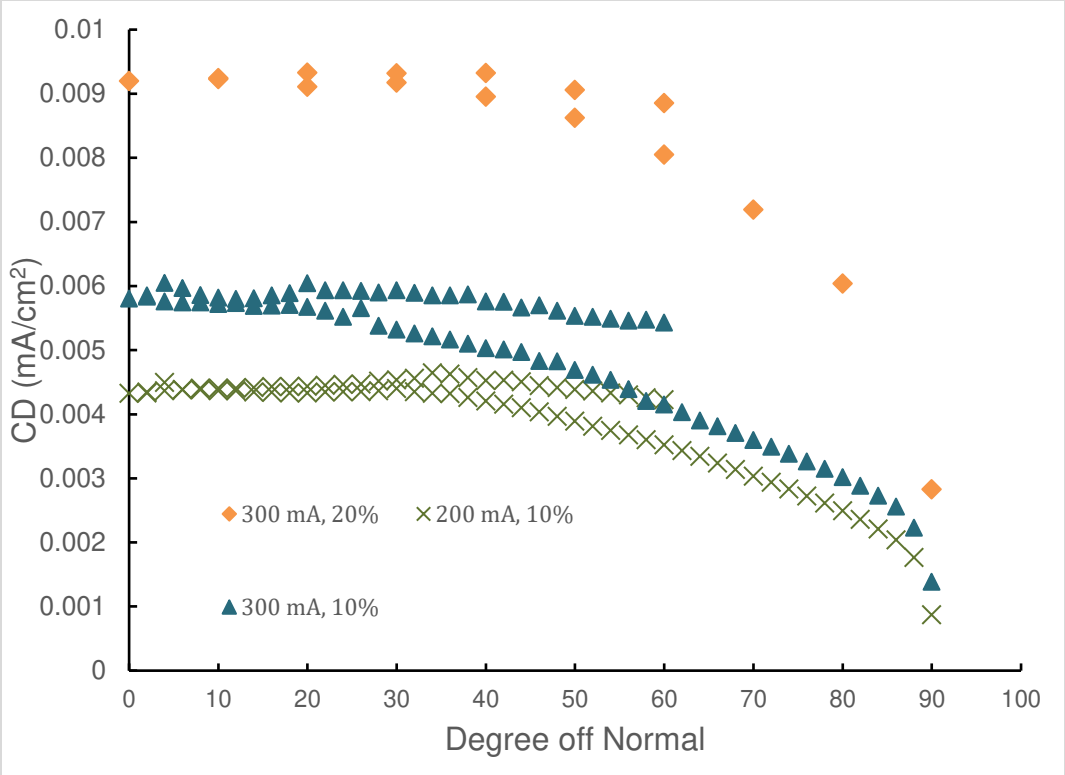

Figure 4.1-4: Plot of Current density in mA/cm^2 versus zenith angle for 200 and 300 mA at 10% Utilization States and the 300 mA at 20% Utilization

Section 4.2 - Ion Current Production

An approximate ion production current can be found using the CD curve fit method described in Section 4.1. Fitting a curve to current density data from the 300 mA 10% utilization target operation state gives Equation 4.2-1 which has x, the angular position, in radians.

$$f(x) = -(7.994074e-03) * x^3 - (5.078270e-3) * x^2 + (2.067307e-3) * x + 5.809506e-2$$

Equation 4.2-1

Putting the equation in the double integral for the assumed azimuthal symmetry yields Equation 4.2-2 for calculation of the ion production current. This equation uses φ for the azimuthal axis. When integrated with a constant probe distance r of 0.71 m this equation gives a total ion production current estimate in units of ampere.

$$\int_0^{2\pi}\int_0^{\pi/2} (-(7.994e-03)*x^3-(5.078e-3)*x^2+(2.067e-3)*x+5.809e-2) * \sin(x) * r^2 \, dx d\varphi$$

Equation 4.2-2

The ion production current from this method for this state is 0.136 A or 136 mA which is 60% below the target ion production current, however this result is not corrected for attenuation from charge exchange collisions. Under this operating condition, we measured a background pressure of 5.6E-05 Torr and we used this pressure to determine the neutral density required in the charge exchange correction (Equation 4.1-1). Subsequently, we calculated the ion production current to be 267 mA, which is within 11% of the target current that was set for this condition using a pulsing technique described in the next section. We note that there is some ambiguity in the neutral pressure as the ion gauge used to measure chamber pressure is suspected of reading low. With an assumed worse case of the pressure being twice as high as recorded, the total ion current becomes 525 mA, which highlights the sensitivity of the correction factor to the chamber pressure for CD-based calculations of the ion production current.

As mentioned above, total ion production currents were also measured for all states by pulse biasing the HAPC relative to the vacuum chamber walls. This allows the entire chamber to act as a collector for the emitted ions as the pulse voltage used acts to repel all the electrons that would otherwise flow to the wall and so provides a direct measurement of the ion production current. A source of error in this measurement however comes from ion induced secondary electron emission from the biased chamber wall. This makes the measured current in the pulsing technique larger than the actual collected ion current as the emitted electrons moving away from the chamber wall that collect on the HAPC appear in current measurements the same as if ions are moving toward the chamber wall. Correcting the measured currents for the IISEE current can be done in a similar manner to how CD probe measurements were corrected using Equation 4.1-3 and multiplying the measured current by the factor K_{SEE}. As most of the surfaces in the vacuum test chamber consist of stainless steel, the IISEE yields used need to reflect that and so a yield of 0.1 was assumed for singly charged ions and 0.3 for doubly charged ions, with assumed

current fractions of 0.95 for singles and 0.05 for doubles. It was assumed that all ions created in charge exchange collision are also collected, which eliminates the need to correct the pulsed measurement for that process.

The IISEE yield for singly charged krypton ions on stainless steel was estimated. This is because yields for Kr ions on stainless steel do not exist while Kr ions on tungsten and molybdenum have extensive experimental yield data to draw upon. Modeling electron emission on iron and tungsten surfaces with noble gas ions shows similar yields of less than 0.1 when ion energy is below 500 eV [22]. Experiments using Xenon also show similar yields between stainless steel and molybdenum for ion energies below 500 eV in the range of 0.02 to 0.04 [26]. Other experimental data using sodium ions shows yields ranging from 0.001 to 0.1 for ion energies between 100 eV to 250 eV on stainless steel surfaces [27]. With these data in mind the yield of 0.1 was assumed as the worst case IISEE yield in testing the HAPC for singly charged ions. For doubly charged ions a yield of 0.3 was assumed based off tungsten yield data. The current fractions for each charge state used were based on the measured species fractions of the HAPC discussed later in section 4.8.

The IISEE corrected ion production currents measured in the above tests were used to make adjustments to the anode current operating points to set the operational states for the B-SPICE mission close to the desired ion production currents. Limited amounts of time for delivery of the HAPC for B-SPICE integration at the University of Michigan unfortunately resulted in some states not getting the refinement needed to get the ion production currents within 5% of the target current. Figure 4.2-1 shows ion production currents plotted versus anode current for each operational state with the krypton flow rate called out in the legend.

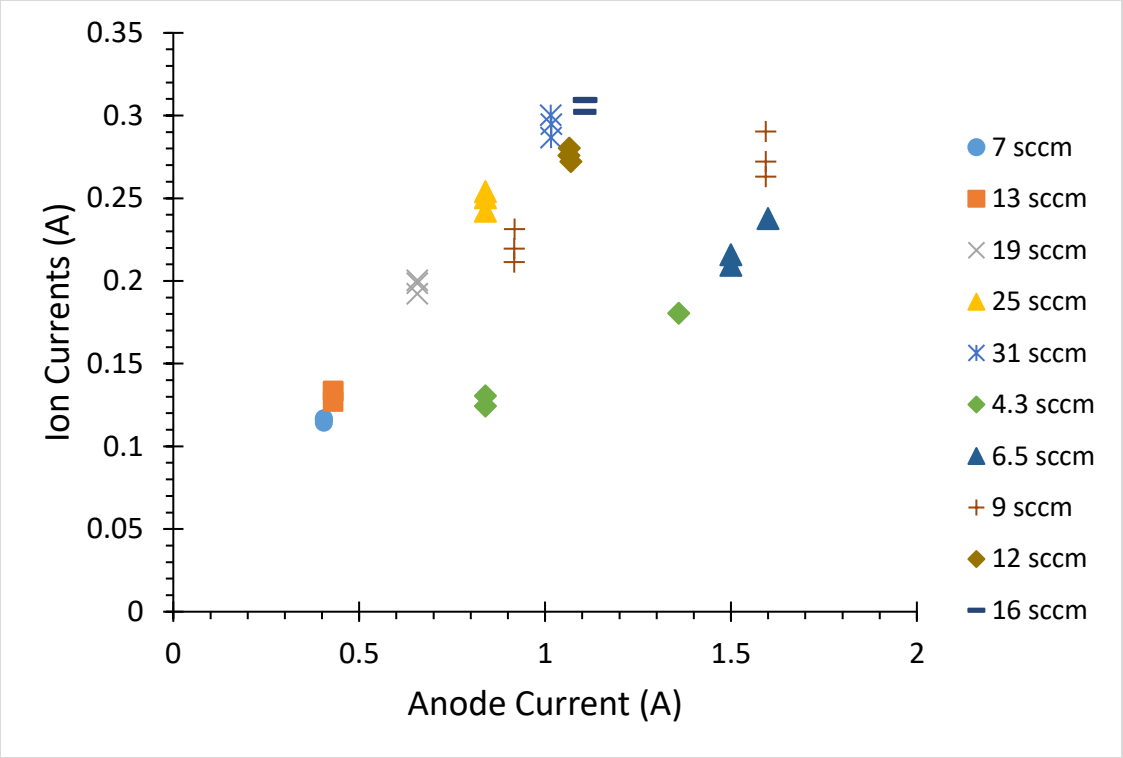

Figure 4.2-1: Ion Production Currents for BSPICE Flow Rates at given Anode Currents.

The states targeting 30% utilization efficiency also saw issues in voltage limiting of the anode power supply. This was because the anode power supply used in the HAPC electronic box for the sounding rocket mission was unable to reach a voltage level capable of producing the needed currents to reach the target ion production currents. The 300 mA and 250 mA at 30% utilization (the 6.5 sccm flow and the higher current 9 sccm flow conditions) only marginally fell short of the targets while the 200 mA at 30% (4.3 sccm flow) condition fell well short. The 20% utilization 200 mA and 250 mA state (lower current 9 sccm and 12 sccm) also see some fall off in ion production current.

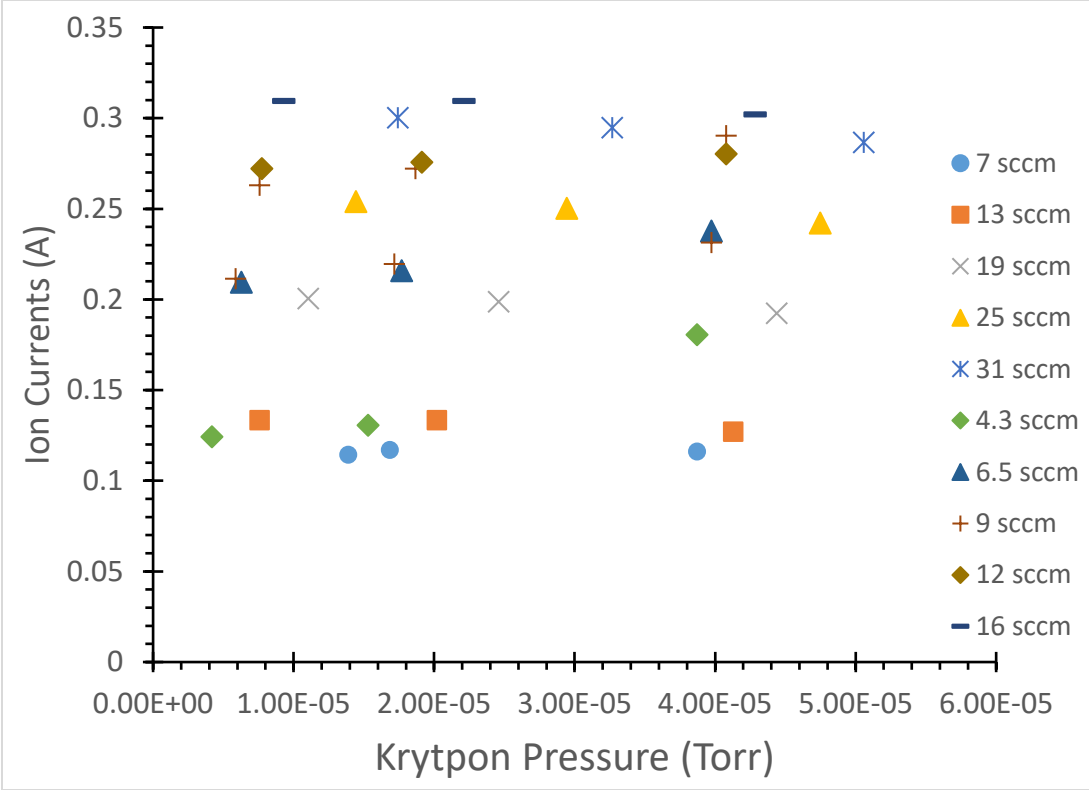

Figure 4.2-2: Ion Production Currents for BSPICE Flow Rates at Krypton Pressures in Chamber

The drop in actual ion production current relative to our targets occurred at lower flow rates and higher utilizations with corresponding lower chamber pressures as seen in Figure 4.2-2 with the 4.3 and 6.5 sccm flow rates. This is of some concern for B-SPICE though, as the rocket flight trajectory carries it through regions of space that are far lower in pressure than our ground-based test facility can achieve. This leads to the question of whether the HAPC can operate at certain ion production currents and utilizations above certain altitudes. It is possible that the ongoing analysis of the BSPICE flight data will shed more light on this issue.

The actual utilization for each state can be calculated in the ground-based tests presented herein using the measured ion production currents and pressure transducer readings from the feed system. The HAPC flow rates are calculated from the reported transducer pressures in the feed system using the choked flow calculation in Equation 2.2-1 and then the flow rate is converted to units of Aeq. The conversion to Aeq is shown in Equation 4.2-3 below.

$$\dot{m}(Aeq) = \frac{\dot{m}\left(\frac{kg}{s}\right) * (1.6 * 10^{-19})(C)}{M(amu) * (1.66 * 10^{-27})(\frac{kg}{amu})}$$

Equation 4.2-3

With these two equations, calculating the HAPC utilization is simply dividing the ion production current by the sum of the HA and HC flow rates in Aeq. Doing so gives the HAPC utilizations shown in Table 4.2-1 below.

Table 4.2-1: Actual Utilization and Ion Production Currents for B-SPICE States

Target Utilization	**10%**					**30%**			**20%**		
Target Current (mA)	**100**	**150**	**200**	**250**	**300**	**200**	**250**	**300**	**200**	**250**	**300**
Actual Current (mA)	114.3	133.3	200.5	254.0	300.3	124.3	209.5	263.1	211.4	272.1	309.3
Actual Utilization (%)	8.60	7.77	9.71	10.08	10.37	11.33	17.35	18.86	15.16	16.03	16.32
Anode Utilization (%) (anode flow only)	18.84	13.40	14.92	14.13	13.82	33.15	43.15	39.10	31.43	27.90	26.35

The main takeaway from the tabulated data is that our set points fell short on the utilization targets of 20% and 30%, however, we point out that this was largely due to a change in the cathode flowrate setting to a higher value that was made during B-SPICE integration testing. The cathode was having trouble igniting due to insufficient elevated flow durations, but at the time this situation was not recognized. To achieve reliable ignition during integration testing the cathode flow rate was increased from 5 sccm to 10 sccm, and this change wasn't reverted once the culprit of the starting issue was resolved. Running calculations using the original ideal 5 sccm on the cathode and the recorded test flow rates of the anode gives utilizations that match much better with the targets. When we use the lower cathode flow rate the SSQ1 operational states end up having most utilizations at 11% with one at 9.86%. And the SSQ2 states with a target 20% are all within 0.5% of the target. Only the 30% SSQ2 states fall noticeably short of their target at around 25% for the 250 and 200 mA states when the original, lower

cathode flow value is used. The 300 mA state for 30% utilization struggled to reach its target anode current and fell well short of it, which resulted in a utilization efficiency of only 17% due to inadequate anode voltage capabilities of the flight power supply. Had it managed to achieve the target anode current under the available voltage from the anode supply, the state would have achieved about 27% utilization calculated with the lower cathode flow rate.

Section 4.3 - Plasma Plume Characterization: Plasma Potential

The following sections contain discussions of data collected with the Langmuir probe (LP). There is quite a bit of details in these sections and so a quick summary is provided here. The goal of the LP measurements was to collect plasma property data in the region between 30 and 70 cm downstream of the HAPC for use as inputs by plasma simulations conducted at LANL. The plasma potential was found to fall between 13 and 22 V relative to the cathode potential, which was tied to the chamber wall for these tests. The electron temperature was between 0.6 to 1.2 eV, and the electron density displayed the expected drop off of 1/r2 with distance and proportionality with the given ion production current.

In this section we present details concerning the plasma potential measurements. A key plasma characteristic that Langmuir probe trace analysis can provide is the plasma potential, found as the potential at which the current collection mechanism measured by a LP changes from the electron retarding region to the electron acceleration (or saturation) region [9]. A common way of finding this potential and the way used for the HAPC LP traces, is to create a fitted curve in each of these regions and find the intersection point of these curves, which is taken as plasma potential. Figure 4.3-1 demonstrates this with SSQ1 data using a Langmuir probe analysis program available at CEPPE. Here the saturation region gets a linear fit while the retarding region has an exponential fit. Note that the current is plotted on a logarithmic scale so the linear fit region appears curved and the exponential region appears linear. Another method for finding the plasma potential is to use the 1st derivative of the LP current relative to its voltage, and the potential where the derivative is a maximum is taken as the plasma potential [14].

The LP analysis used herein also assumes that seven requirements of the plasma are met. These are: 1) cold ions, 2) electrons at or near thermal equilibrium, 3) collisionless plasma, 4) electrostatic conditions (no rapid time varying processes are occurring), 5) non-magnetized, 6) quasi-neutral, and 7) isotropic and homogenous [14].

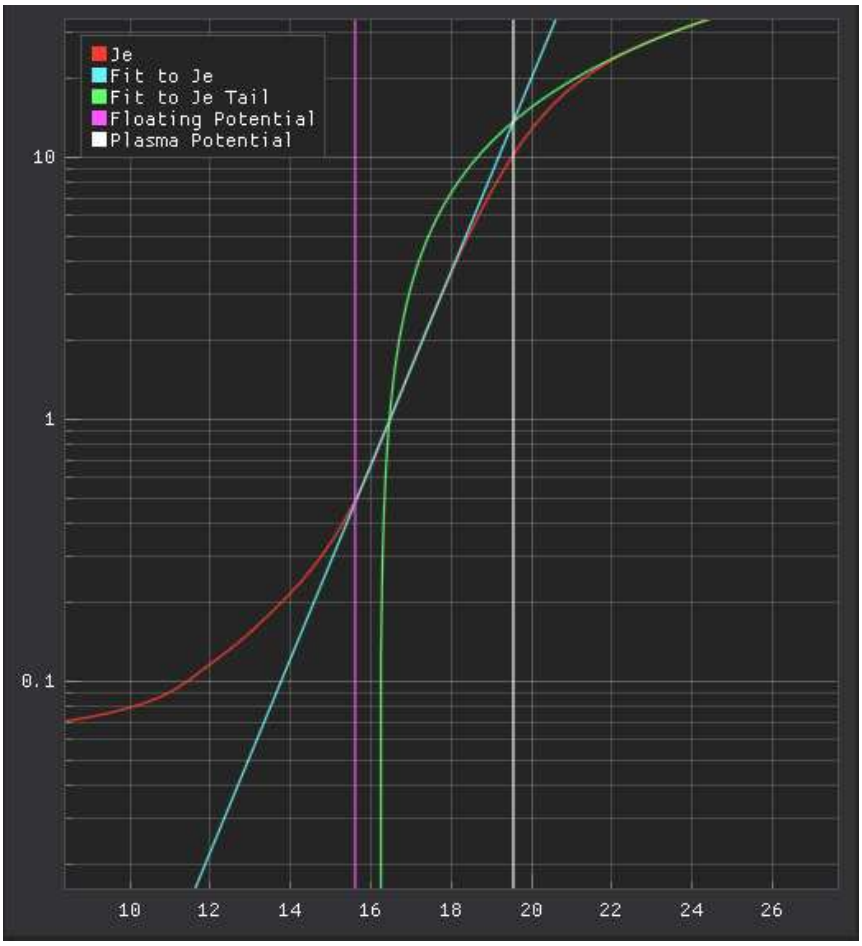

Figure 4.3-1: Fitted Curves on an LP Trace for the SSQ1 state of 300 mA Target Current

As mentioned above we used the two-fit, intersection method to obtain plasma potential data, and these measurements are plotted with respect to distance as shown in Figure 4.3-2. All operational states display a trend where the plasma potential decreases with increasing distance as would be expected in a freely expanding plasma, with two exceptions. The states with 250 mA and 20% and 10 % utilization targets show the furthest measured plasma potential slightly higher than the middle measurement. This could be due to minor fluctuations in operation while taking the traces or due to measurement error,

which wasn't estimated rigorously due to time constraints that prevented multiple repeat tests to be conducted at several operational states. A rough judge of error in the plasma potential found using the intersection method when a plasma is relatively quiescent is to use $\pm T_e$, the electron temperature in eV, which was about 1 eV under the 250 mA operation state. This rough rule of thumb ($\pm$1 V) places the variations observed in most measurements to be within the margin of error even though the trends in the data appear to be clearly delineated. Error bars are not displayed on the plot to reduce clutter. Regardless, we note that both of the non-conforming data sets, the ones with higher plasma potential at further distances, have a target ion production current of 250 mA.

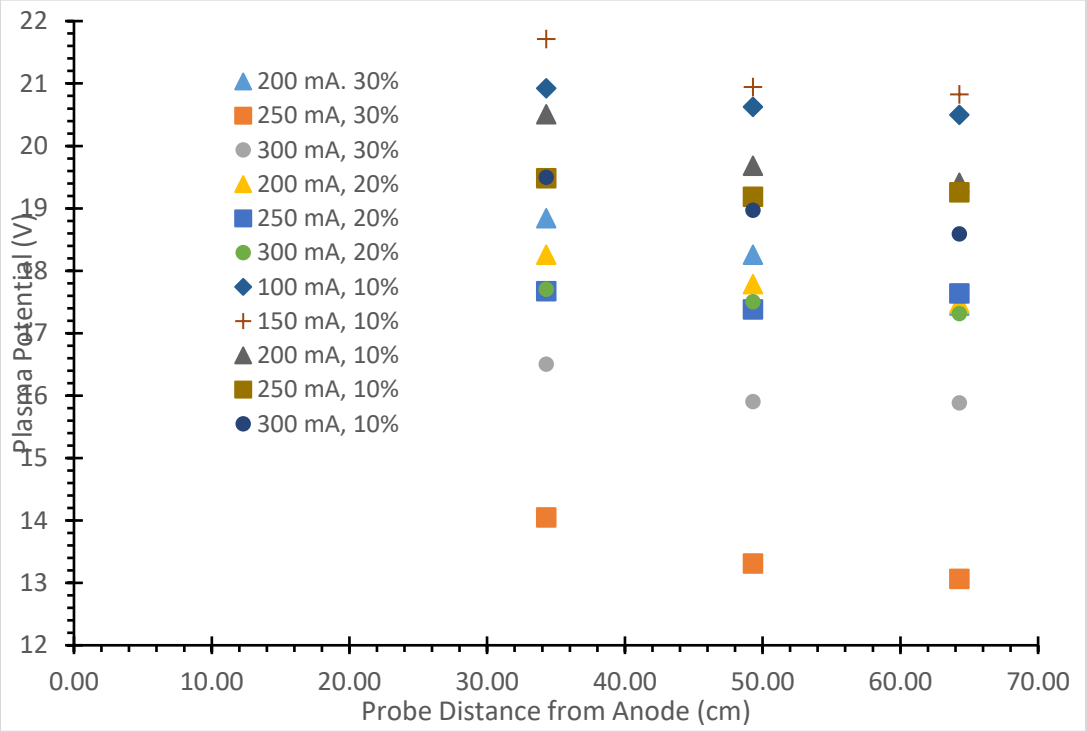

Figure 4.3-2: Plasma Potential w.r.t Distance of All B-SPICE States

The 20% utilization states have a tight grouping of plasma potential with a maximum difference of about 1.1 V while the SSQ1 states have a maximum difference of 2.2 V. The 30% target utilization states of SSQ2 saw the broadest difference of ~4.8 V. We believe the variation in plasma potential with distance is likely driven by the electron temperature if the Boltzmann condition applies to our expanding

plasma, but this result isn't strongly supported by electron temperature measurements that are presented in the following section.

Section 4.4 - Plasma Plume Characterization: Electron Temperature

The electron temperature is another plasma characteristic discernable from LP traces. It is typically calculated as the inverse of the slope of the linear section of the electron current when it is plotted on a log scale as discussed in the LP literature [14]. The electron current in a LP trace is determined by finding a fit to the ion saturation characteristics of the trace at highly negative biases and then subtracting the fit from the LP current. This is important to do when plotting the LP electron current on a log plot because one needs to accurately discern the electron current in regions of the trace where net collection of ion currents is on the same order or exceeds the current of electrons flowing to the probe. The reader is referred to the LP literature for more details concerning the conventions of accurately subtracting the ion current signal and determining the electron current to a probe.

The electron temperatures varied over the range from 0.57 eV at the lowest to 1.15 eV at the highest over the distance between ~30-70 cm over all the operational states tested. The error in electron temperature measurement is presented below to be about $\pm$0.2 eV, and our measurements suggest that the temperature isn't constant in the plasma expansion region. At the closet distance electron temperatures are higher and vary over a smaller range from 0.75 eV to 1.15 eV. Electron temperature was found to decrease with increasing distance and ion production current but has an inverse relation with increasing utilization efficiency, which was surprising because higher utilization at a given ion production current typically results in lower vacuum chamber pressures and lower neutral densities normally correlate to higher electron temperature. This unexpected result is clearer to see with the 300 mA operational state that in Figure 4.4-1 below all have circle markers, with the 10% state having the highest electron temperature and the 30% state the lowest. Another phenomenon noticed is that three operational states have a lower electron temperature at the middle measurement distance. Specifically the 10% utilization

efficiency operational states at 100 mA and 150 mA as well as the 200 mA at 30% state all have the middle-distance electron temperature as their lowest. The 100 mA state has the middle and furthest temperatures close enough that this discrepancy can easily be attributed to measurement error, which is roughly estimated to be ±0.2 eV. This error is due mostly to the analysis step involving the subtraction of the ion saturation fit because the electron temperature is sensitive to the choice of the range of voltages used to obtain the fit.

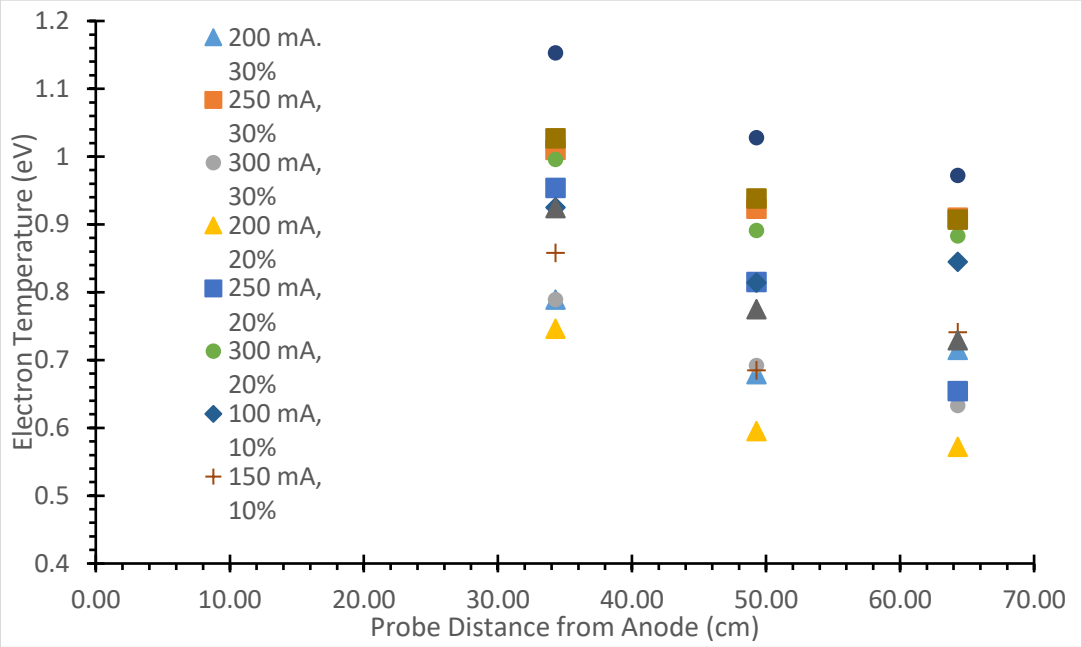

Figure 4.4-1: Electron Temperature w.r.t Distance for all B-SPICE States

All LP traces showed another feature that was expected at the relatively low background pressures of our studies and is shown in Figure 4.4-2. An additional section in the electron retarding region at negative bias appears to vary linearly if the plot were changed to a linear-linear style (but is curved on a logarithmic plot). This could indicate a second, hotter, non-thermal electron population present in the plasma in some operating conditions. The linear behavior with probe bias suggests that this group represents a primary electron population that is derived from electrons emitted directly from the cathode and accelerated into the expanding plasma regions that have not been thermalized.

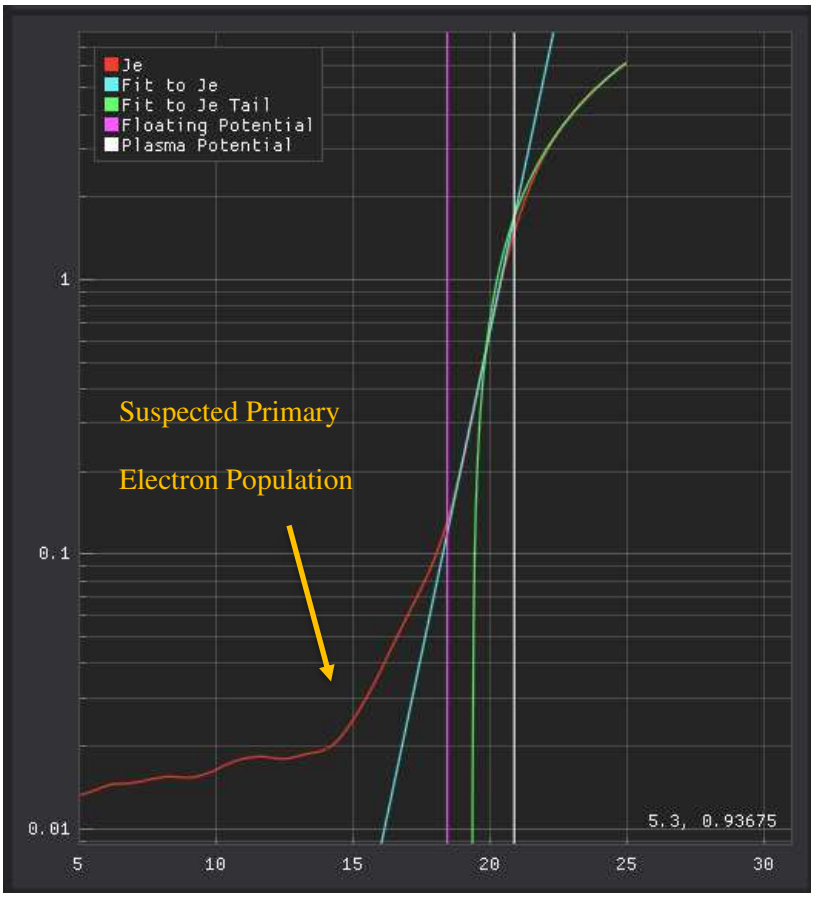

Figure 4.4-2: LP Trace Showing a Second Electron Population is Present

Investigating the 100 mA state LP trace at the closet distance further illuminates this result. Here we used an approach from Beattie to fit both primary and Maxwellian electron population properties to the LP electron [28], and

Figure 4.4-3 shows the fit plot superimposed over the raw data. This fit allows us to obtain an estimation of the density and temperature of the primary and Maxwellian electron populations to be 8.0e+04 1/cm^3. and 27 eV and 1.81e+07 1/cm^3, and 0.93 eV, respectively. The energy of the primaries was expected to be about equal to or no more than the potential difference between the plasma potential (21 V for this operational state) and the cathode potential, which is just the plasma potential because the cathode was grounded. The primary energy from the fit of 27 V is greater than 21 V, but roughly in agreement. As the primary electron density is quite small compared to the thermalized population it can

be assumed that our previous analysis assuming only Maxwellian electrons is adequately accurate for representing the HAPC plasma plume and the primary electrons can be ignored.

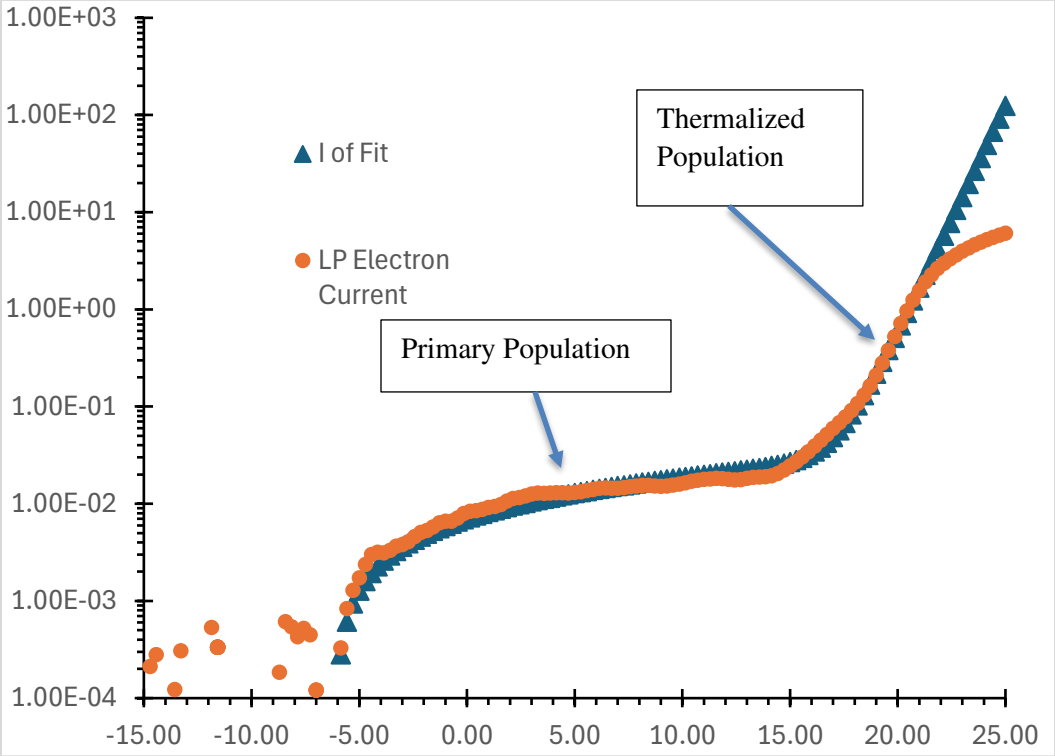

Figure 4.4-3: LP Electron Current and Fitted Current as Functions of Probe Voltage Showing Presence of Primary Electrons in the Plasma Plume expanding from the HAPC.

Section 4.5 - Electron Density

The final plasma characteristic taken from analysis of the LP traces is the electron number density. As demonstrated in the electron temperature section, electron density can be used in plasma modeling formulas to predict behaviors in the plasma and extrapolate values for regions of the plasma plume not directly measured. Figure 4.5-1 below shows the measured electron densities, which is proportional to the electron current when the probe is at plasma potential. This current is found using the fits of the thermalized linear section of the electron retarding region as discussed with the electron temperature and extrapolating this curve to the plasma potential. The clearest trend is the falling density

with increasing distance. The density reduction with distance nearly matches the expected $1/r^2$ trend (as shown by the solid line in the plot) with some scatter, but we believe measurement errors caused by using the two-fit interception technique to determine plasma potential and subsequently the electron saturation current can explain some of the deviation from $1/r^2$ behavior. Charge exchange reactions will also cause a deviation from $1/r^2$ behavior because they have to effect of reducing the effective energy of the expanding ions. We also note that electron temperature changes with distance, and this can also impact the density-distance behavior. The states with a target utilization efficiency of 20% have the highest scatter across the three distances measured. Importantly, the SSQ1 states generally follow the expected $1/r^2$ behavior, which we recommend using in the simulations being performed by LANL. We also note that some of the discrepancies observed in Figure 4.5-1 may stem from the anode orifice eroding (becoming larger) during testing of SSQ2, as opening of the orifice diameter reduces ion production current.

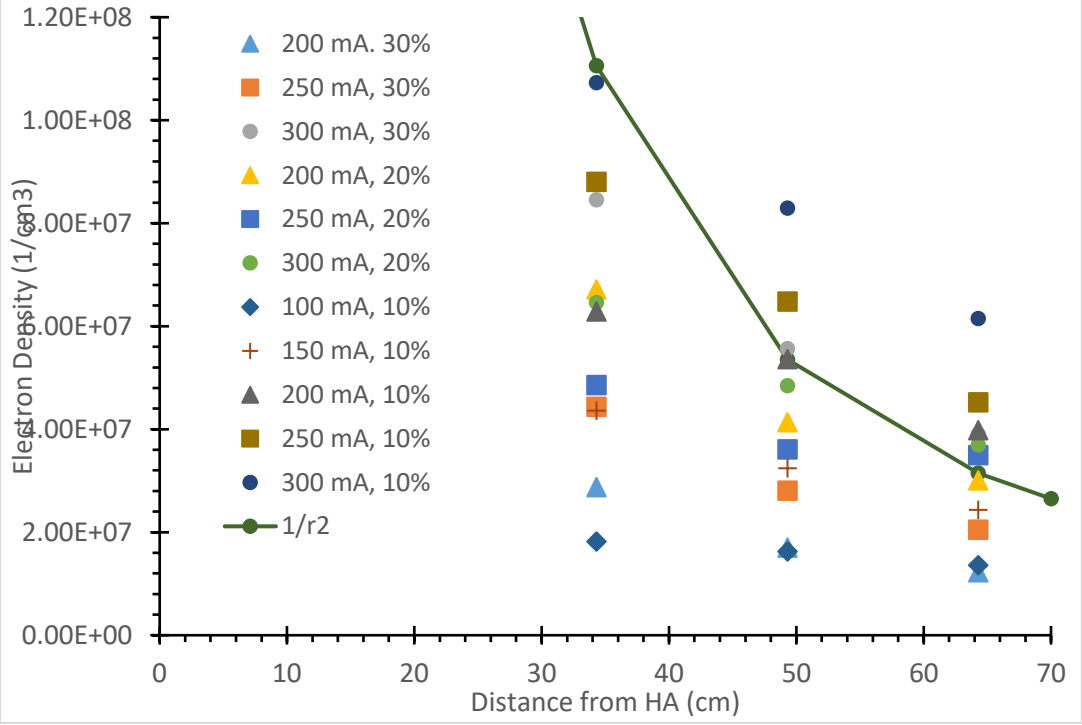

Figure 4.5-1: Electron Densities w.r.t Distance for Thermalized Electron Population in All B-SPICE States.

Section 4.6 - Plasma Plume Characterization: Ion Energy Distribution

Ion energy distributions (IEDFs) found using both an RPA and ESA showed strong agreement in the peak ion energy (most probable ion energy), which was also found to be strongly correlated with and nearly equal to the measured HA voltage. For comparison, the SSQ1 state of 300 mA and 10% utilization targets saw peak energy measured at 74 E/q with the RPA and 72 with the ESA part of the E-Vader, the HA voltage reported for the ESA test was 81 V and for the RPA was 79 V. Figure 4.6-1 shows the RPA and ESA traces for three of the SSQ1 states together, showing the 100 mA state has the strongest agreement between the RPA and ESA peak energy and is predicted by the anode voltage at 155 V similar to the 300 mA state. The 200 mA state has peak energies of 88 E/q and 97 E/q while the HA voltage reported 95 V to 100 V consistently. This indicates that while variation in operating condition can vary the ion energy, the anode voltage is a reliable predictor of the peak energy. Peak ion energies being nearly equal to the anode voltage was an expected result as most of the ions are believed to be produced very close to the HA orifice, and the potential difference through the orifice to the anode isn't expected to be very large due to the high conductivity of the plasma here.

SSQ2 states show greater difference in peak energy between the ESA and RPA measurements but this is believed to be due to orifice differences changing the HA operating voltage. As example the 200 mA at 20% operational state has peak energies at 162 E/q and 134 E/q for the ESA and RPA respectively, with the HA voltage reported for each were 167 V and 140 V. The HA voltage dropped from 167 V to 140 V over the time the RPA and ESA data were collected due to HA orifice enlargement during the test. Conversely, the ESA and RPA traces for some SSQ2 states, specifically the 200 mA 30% condition, a strong agreement was observed between the RPA and ESA data, but in this case was due to voltage limiting of the power supply at that condition. In conclusion, although all SSQ2 states do not have exact agreement between the ESA and RPA data for the peak energy, the measured anode voltage during either ESA or RPA testing show the anode voltage within 10 V of the measured peak energy for each current and utilization condition.

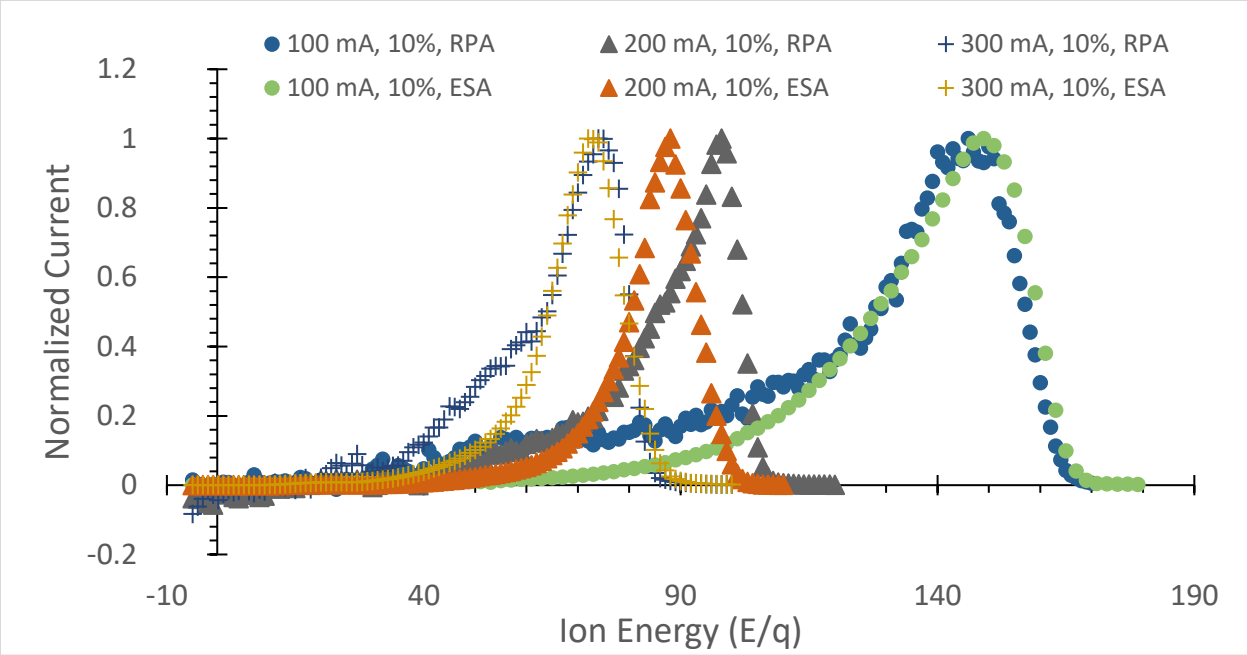

Figure 4.6-1: RPA and ESA traces for SQQ1 States with 100 mA, 200 mA, and 300 mA Target Ion Currents

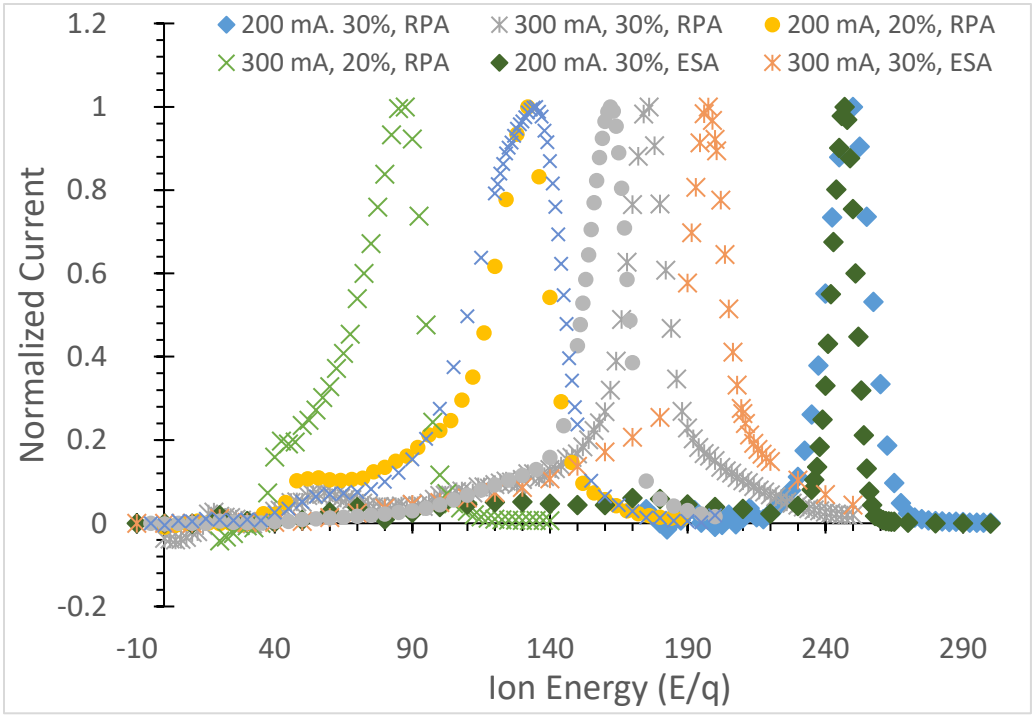

Figure 4.6-2: ESA and RPA traces for SSQ2 States of 200 mA and 300 mA currents

The observation that the peak ion energies are consistently close to the HA potential with some ions in the tails of the distribution at energies higher than the peak energy is similar to observations in HTs. An explanation of ions with higher-than-expected energy is an active area of research in HTs and other plasma sources and is beyond the scope of this thesis, but we speculate below about the peak energy and ions detected at energies below the peak. As mentioned above, the most probable or peak energy being lower than the HA voltage is due to the primary ionization region likely being at a slightly lower voltage than the anode as this region is assumed to be located at the orifice exit or just outside the orifice. The peak energy being slightly lower than the anode voltage could also be due to collisions of ions with each other and neutral atoms—thermalizing the energy distribution. The tail of lower energy ions observed for all the operational states are likely from collisions or contributions from ionization occurring at lower potentials further from the HA and orifice.

Section 4.7 - Plasma Plume Characterization: Drift Velocity

The drift velocities of the ions were calculated from the measured peak or most probable ion energy. The drift velocity is associated with the peak energy with a spread in velocity taken from the spread in measured energies using the full width at half-maximum, as shown in Figure 4.7-1 for the 100mA state. With normalized currents used on the energy traces, the spread in drift velocities come from the width of the curve at the normalized current is 0.5. The velocity, v, is then calculated using Equation 4.7-1.

$$v = \sqrt{\frac{2ez}{m_i M}\mathrm{E}}$$

Equation 4.7-1

Here e is the charge of the ion at 1.6e-19 C, m_i is the atomic mass of an ion, 83.8 amu for krypton, M is 1.66e-27 kg/amu, z is the ion charge state, and E is the ion energy in E/q. With units of E/q being energy per charge and then multiplied by e and the dimensionless z giving the units of Joules. Because of

this, singly and doubly charged ions have different velocities despite experiencing the same energy per charge accelerating them. The averaging of energies from the ESA and RPA traces were used for calculation of velocities.

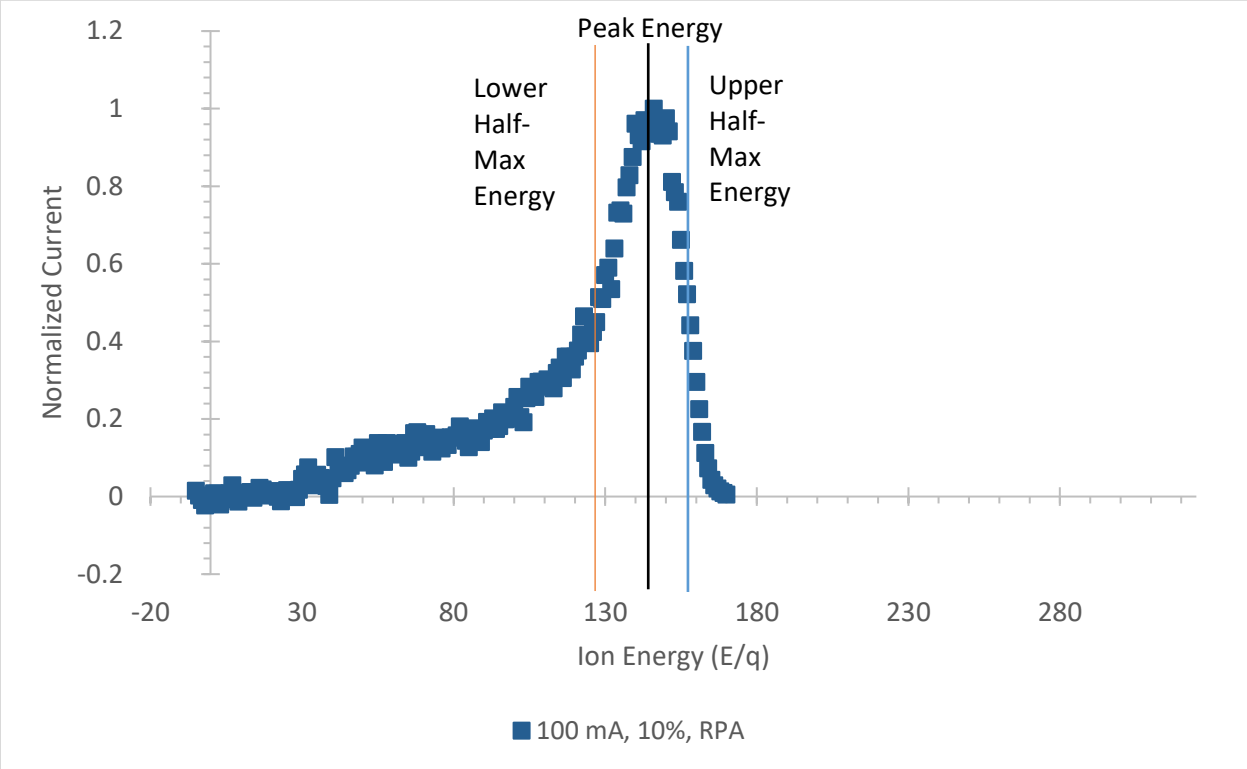

Figure 4.7-1: ESA Trace for the 100 mA State with the Half-Maximum Energies Marked

Calculating the velocities for the singly charged ions for all B-SPICE states has ion velocity ranging from ~13 km/s to almost 24 km/s. Figure 4.7-2 shows the drift velocities for the singles with respect to the ion production current. The error bars represent the spread in velocity calculated from the half-maximum-width energy. In the positioning of the x-axis ion production current, the error bars are set to encompass the ideal ion current targets and the measured ion currents from section 4.2.

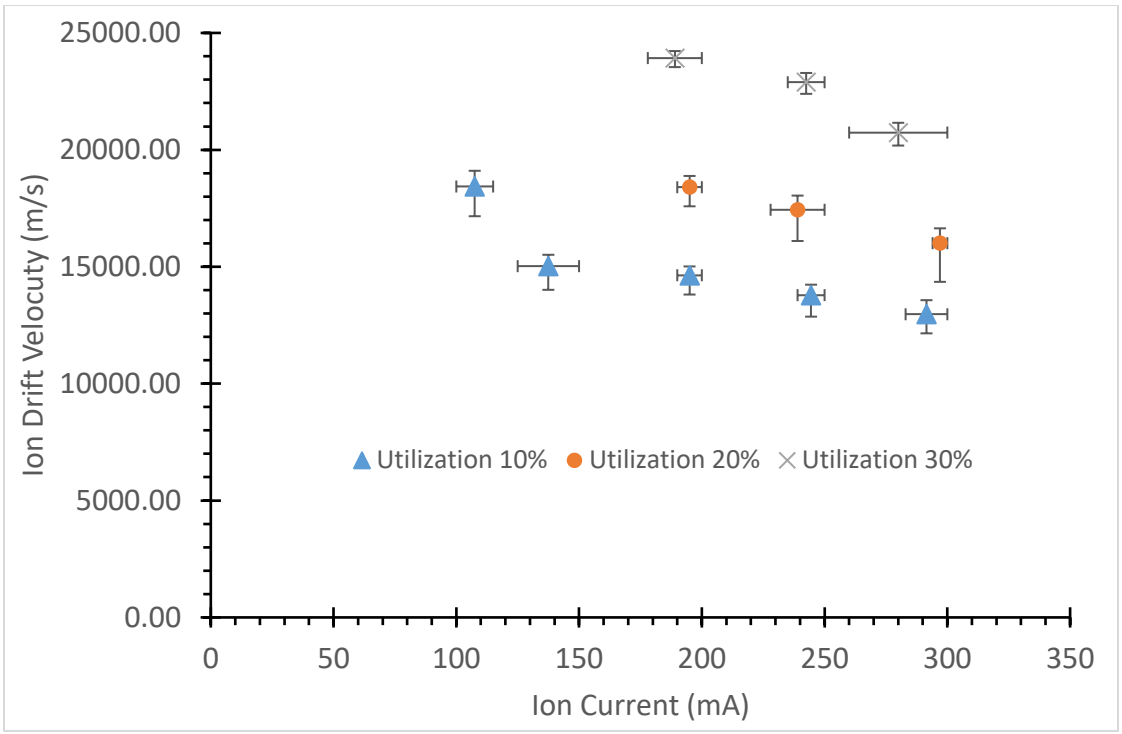

Figure 4.7-2: Ion Velocities at the B-SPICE Ion Currents for Singly Charged Ions

The results of doing the same calculations for doubly charged ions are shown in Figure 4.7-3. With the larger charge per ion for doubles, the resulting velocities are greater than those of the singles.

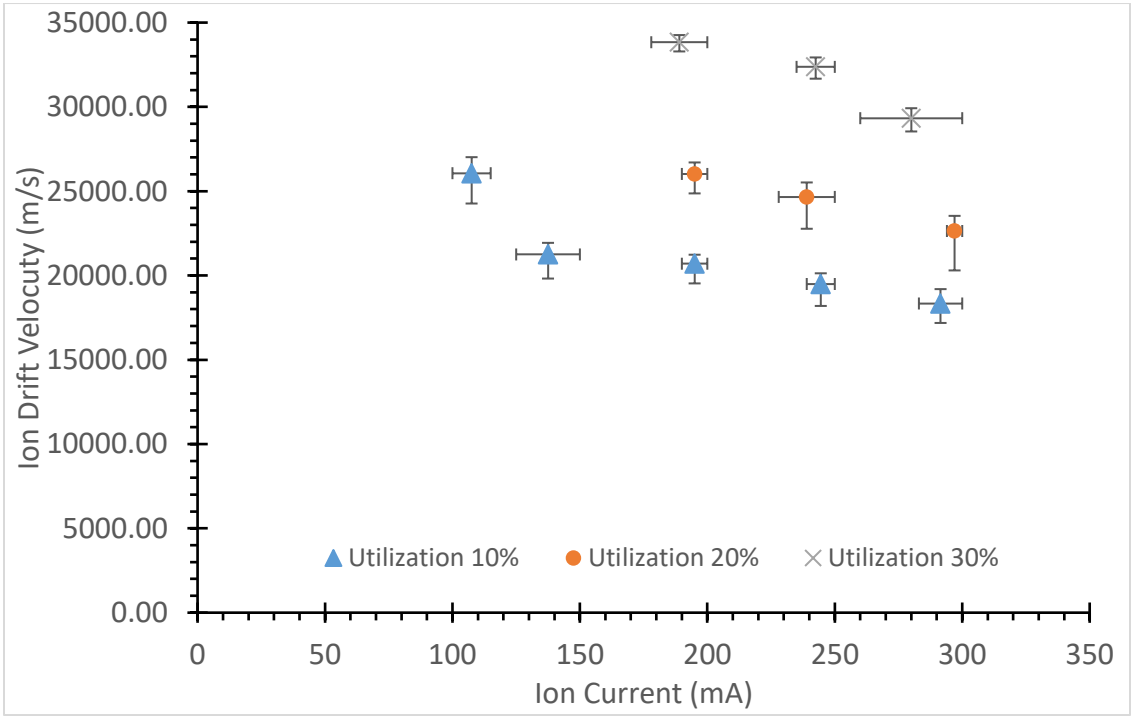

Figure 4.7-3: Ion Velocities at the B-SPICE Ion Currents for Doubly Charged Ions

Section 4.8 - Charge State Fractions

Charge state fractions were calculated from a curve fitting technique based on the method described in Huang and Rohit, with the technique implemented in a Python code program written by Dr. Shawn Farnell at CEPPE [20]. The method involves making bi-gaussian fits sequentially to each peak in the ExB spectra individually starting with the largest peak, then subtracting out the result before moving to the next peak. Each peak corresponds to an ion species, ideally the different charge states of the propellant, although contaminants from the facility can show up in the spectra. As peaks are fitted, integrating under each using the fit is done using the 'Quad' integration function from the SciPy Python code module. With the areas under each peak calculated, the area fractions, species fractions, and current fractions of the spectra can be calculated. Charge state fractions are reported herein from the species fractions calculated.

Charge state fractions for operational states of SSQ1 were taken at discrete ion energies using the E-VADER providing insight into what energies have what charge states. The discrete energies where data were taken consisted of the peak energy, the two energies associated with the currents measured at half the maximum current, and a fourth energy corresponding to the lower energy tail of the energy distribution. The tail energy was taken at an energy below the lower energy of the half-maximum point. Specifically it was selected as the energy of the lower half-maximum point minus the difference between the energy of the peak and the lower energy half-maximum point.

Singly charged ions were the primary charge state present across all energies, although ExB spectra taken at ion energy per charge state at the lower half-max energy and peak energy generally contained non-negligible concentrations of doubly charged ions. The leading half-max energy consisted almost entirely of singly charged ions, averaging at 99% singles across each ion production current. The lower energy ExB spectra taken at the tail energy sees a varying amount of doubles based on the ion production current, with the 300 mA state having 9% doubles present while the 150 mA state had 0.31%

doubles. The remaining fractions for 100 mA, 200 mA, and 250 mA were 3.75%, 3.82%, and 4.44% respectively.

Triply charged ions were almost absent outside of some low level signals that do not give a clear indication of a pattern in their concentrations except for the 100 mA state. The 100 mA 10 % utilization state saw the highest triple fraction of SSQ1. We note that this 100 mA state had the highest anode voltage and ion energy suggesting that electrons exist with energy necessary to create triply charged ions.

To get an estimate of the charge state fraction of a population, weighted averages were taken of each charge state fraction across the four energies measured. The weights, w_n, were found using the measured current from the ESA trace at each chosen energy, I_n, and finding its fraction of the summed currents, $w_n = I_n/I_{tot}$. The overall charge state fractions, CSF_O, were then a sum of the specific charge state fractions, CSF_n, multiplied by their weight, $CSF_O = \sum CSF_n * w_n$. Table 4.8-1 below shows the resulting overall charge state fractions from this method.

Table 4.8-1: Overall Charge State Fractions for SSQ1 States

	100 MA	150 MA	200 MA	250 MA	300 MA
SINGLES	0.9302	0.9745	0.9603	0.9666	0.9503
DOUBLES	0.0683	0.0255	0.0395	0.0345	0.0497
TRIPLES	0.0015	0.0000	0.0002	0.0005	0.0000

As can be seen for SSQ1 operational states the ion population consists of almost exclusively singles. The increase in doubles and triples at the 100 mA state, also the highest ion energy and anode voltage state for SSQ1, indicates that higher anode voltages may see continued increase in the population of doubles and triples in the plasma plume. This suggestion does hold for the testing of SSQ2 states with the standalone ExB probe, but the increase is not very dramatic with the singles population still holding the majority of ion charge states, 80% or greater. Due to issues with orifice erosion at these high energy states, the SSQ2 states had their ExB spectra taken with the standalone ExB probe to limit the 'on' time and reduce erosion. The ExB results from the SSQ2 states are not the most reliable as the traces are

'messy' with overlapping peaks and a lack of clarity in what peaks correspond to what charge state. This is shown in Figure 4.8-1 with the ExB traces for the 20% utilizations states with 200 mA and 250 mA target currents. Although the data were harder to interpret, the analysis was performed and Table 4.8-2 below holds the SSQ2 charge state fractions

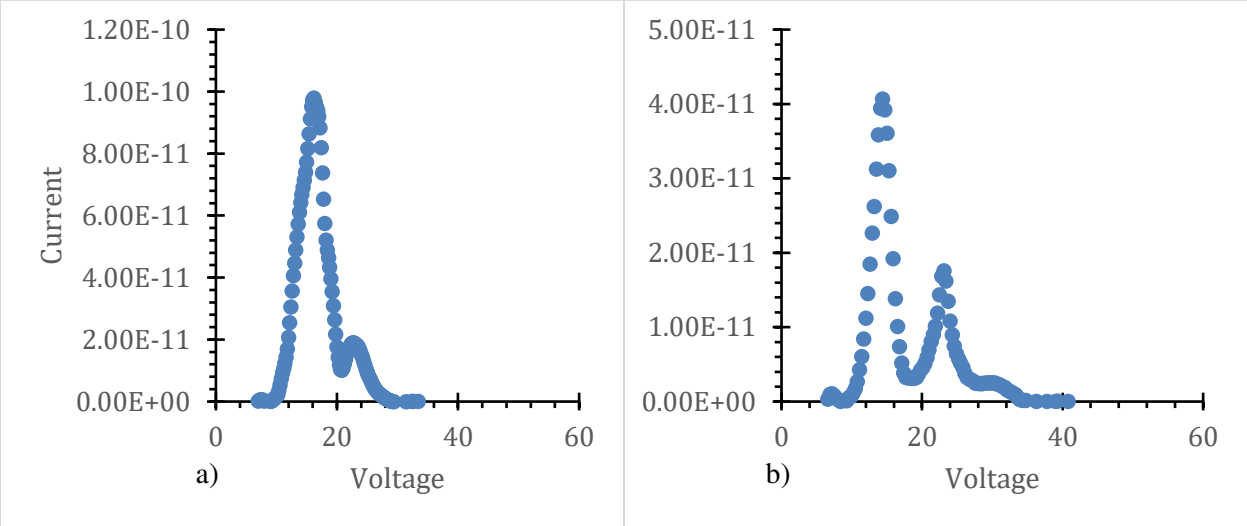

Figure 4.8-1: ExB traces for SSQ2 States 250 mA (a) and 200 mA (b) at 20% Utilization

Table 4.8-2: SSQ2 State Charge State Fractions

	30%			20%		
	200 mA	**250 mA**	**300 mA**	**200 mA**	**250 mA**	**300 mA**
Singles	0.8055	0.8696	0.8874	0.9056	0.961	0.9501
Doubles	0.1679	0.1133	0.1045	0.0913	0.039	0.0499
Triples	0.0266	0.0172	0.0081	0.0031	0	0

Section 4.9 - Anode Orifice Erosion

As mentioned before, the orifice plating hiding the anode is prone to erosion during HA operation, stemming from ions bombarding the orifice and sputtering atoms. The only methodology measuring the erosion of the orifice used was pin gauges for finding the diameter of the orifice after operation. This measurement required that we shut down the vacuum system and vent the chamber for access. The orifice diameter was gauged before and after testing with the plasma diagnostics on every day these types of tests were conducted. Tracking the orifice size with tested states revealed that SSQ1 states did not erode the orifice at rates that would impact the B-SPICE mission. The SSQ2 states, however, showed signs of much greater erosion rates. The erosion of the orifice, and so increasing its diameter, is suspected to impact the ionization performance of the HAPC by simultaneously lowering the anode voltage and the neutral density at the orifice. With a lower neutral density due to a wider orifice, and with less anode voltage biases to accelerate electrons to higher energies the ionization rates may be reduced in turn reducing ion production current and utilization. Testing of the HAPC was focused on the plasma characterization and so study of the orifice erosion was not thorough. Its relevance to B-SPICE rested on performance consistency, so for the mission it was decided with the limited time available it would be accounted for by ensuring a fresh orifice plate was installed before integration, and that it had not significantly eroded during integration testing.

Chapter 5 - Conclusion and Future Efforts

We presented here the characterization of the plasma plume for a Hidden-Anode-based plasma contactor. The HAPC was designed to produce a plasma plume from electron bombardment of neutral gas atoms in a restricted orifice to increase neutral density while having neutral flow rates on the order of less than 50 sccm. Performance along B-SPICE mission requirements was tested, alongside development of a krypton gas feed system. Characterization of the plasma plume was extensive occurring across seven measurement schemes. Five of which used well established probe schemes, a scheme combining two established probes to refine measurements, and a scheme using the vacuum test chamber as a probe surface. Key findings in this work follow.

Current Density sweeps using a Faraday probe established the plasma plume shape as having an under cosine shape whose integration gave total ion production currents after being corrected for ion induced secondary electron emission and charge-exchange attenuation. The physical geometry of the HA is suspected of impeding ion emission at high zenith angles. An asymmetrical shape to the plume lining up with the cathode position next to the anode also suggests a further impediment to ion emission in that direction, which we attribute to higher charge exchange attenuation as ions expanding from the HA that travel through the cathode neutral flow field will be attenuated more than ions flowing in directions away from the cathode axis. Pulse biasing of the HAPC relative to the vacuum test chamber allowed quick evaluation of the total ion production current with direct measurement allowing quicker adjustment of the anode current to match the desired operation states for the B-SPICE mission compared to the time it would take to do this using current density sweeps.

Electrostatic Analyzer and Retarding Potential Analyzer traces confirmed peak ion energy within ~10 V of the measured anode potential. An ExB probe paired with the ESA in the E-Vader probe and a standard ExB probe established plasma charge state fractions with singly charged ions dominating across

tested regimes with a minimum fraction around 80% but predominately at 95% for most operational states.

Langmuir probe traces established plasma potential, electron density, and electron temperature but also demonstrated the presence of a relatively low density primary electron population present. This second electron population is suspected to be minimally significant compared to the much higher density thermalized electron population.

Erosion of the anode orifice was discovered to occur primarily at higher utilizations corresponding with higher anode power and anode voltage. Reduction of ion production with wider anode orifices is suspected indicating future testing should use frequent replacement rates of the orifice plate.

Recommended future work includes thorough characterization of the erosion of the anode orifice and the impact on performance the erosion it has. Redesign work of the hidden anode and hollow cathode device for easier assembly/disassembly for maintenance purposes. Redesign for better locking system of the nut that holds the orifice plate in place. The krypton feed system would benefit from redesigning to reduce potential leak points, use smaller footprint pressure transducers, have simpler routing of tubing and flow hardware, and easier assembly and integration with the HAHC. Future work also recommended is the mapping of the full operational range of HAPC capabilities and plasma plume characterization of that range, and verification of E-Vader and ExB probe results

References

[1] S. T. Lai, Fundamentals of Spacecraft Charging, Princeton: Princeton University Press, 2012.

[2] G. L. Delzanno, J. E. Borovsky, M. F. Thomsen, B. E. Gilchrist and E. Sanchez, "Can an electron gun solve the outstanding problem of magnetosphere-ionosphere connectivity?," *Journal of Geophysical Research Space Physics,* vol. 121, no. 7, pp. 6769-6773, Jun. 2016.

[3] O. Leon, B. E. Gilchrist, G. L. Delzanno, J. D. Williams and G. Miars, "B-SPICE: The Beam-Spacecraft Plasma Interaction and Charging Experiment," in *American Geophysical Union*, San Francisco, Dec. 11, 2023.

[4] D. Goebel and I. Katz, "Fundamentals of Electric Propulsion: Ion and Hall Thrusters JPL SPACE SCIENCE AND TECHNOLOGY SERIES," Mar. 2008. [Online]. Available: https://descanso.jpl.nasa.gov/SciTechBook/series1/Goebel__cmprsd_opt.pdf.

[5] V. Gorokhovsky, "Modeling of DC Discharges in Argon at Low Pressures," in *12th COMSOL Conference*, Boston, 2012.

[6] V. Gorokhovsky, "Filtered Cathodic Arc Method, Apparatus and Applications Thereof". US Patent 9761424, 12 September 2017.

[7] V. Gororkhovsky and S. Robertson, "Low pressure cascaded arc discharge," in *ICOPS*, Denver, Colorado, 2018.

[8] T. C. Tisone and J. B. Bindell, "Low-voltage triode sputtering with a condined plasma: Part I-geometric aspects of deposition," *Journal of Vacuum Science Technology,* vol. 11, no. 2, pp. 519-527, 1974.

[9] R. K. Ham, "An Experimental Invetigation of Heaterless Hollow Cathode Ignition," Colorado State University ProQuest Dissertations & Theses, 2020.

[10] "HCT Custom Cathode Tip," Plasma Controls LLC, 2018. [Online]. Available: https://shop.plasmacontrols.com/collections/cathode-tips-without-heaters/products/hct-custom-hollow-cathode-tip. [Accessed 18 Oct. 2024].

[11] C. Farnell, C. Farnell, J. Williams, D. Williams, B. G. Nguyen, K. E. Greiner and R. K. Ham, "Simplified formation process of a low work function insert". US Patent US10002738B1, 22 03 2017.

[12] K. -I. Oyama, C. H. Lee, H. K. Fang and C. Z. Cheng, "Means to remove electrode contamination effect of Langmuir probe measruement in space," *Review of Scientific Instruments,* vol. 83, no. 5, May 2012.

[13] D. L. Brown, M. L. R. Walker, J. Szabo, W. Huang and J. E. Foster, "Reccomended practice for use of Faraday probes in electric propulsion," *Journal of Propulsion and Power,* vol. 33, no. 3, pp. 582-613, May 2017.

[14] R. B. Lobbia and B. E. Beal, "Recommended Practice for Use of Langmuir Probes in Electric Propulsion," *Journal of Propulsion and Power,* vol. 33, no. 3, pp. 556-581, Apr 2014.

[15] F. F. Chen, "Langmuir probe diagnostics," *IEEE-ICOPS Meeting, Jeju, Korea,* vol. 2, no. 6, 2003.

[16] J. K. McTernan, T. Brubaker and S. G. Bilén, "The pulse Langmuir probe technique to mitigate contamination effects on small spacecraft," in *13th Spacecraft Charging and Technology Conference*, Pasadena, CA, 2014.

[17] B. Ferda, "Retarding Potential Analyzer Theory and Design," Princeton University, Princeton, 2017.

[18] S. T. Lai and C. Miller, "Retarding potential analyzer: Principles, designs, and space aplications," *AIP Advances,* vol. 10, no. 9, 2020.

[19] S. J. Thompsoon, S. C. Farnell, C. C. Farnell, C. C. Farnell, T. M. Andreano and J. D. Williams, "Combined electrostatic analyzer-Wien filter probe for characterization of species distribution in Hall thrusters," *Journal of Applied Physics,* vol. 130, no. 23, 2021.

[20] W. Huang and R. Shastry, "Analysis of Wien filter spectra from Hall thruster plumes," *Review of Scientific Instruments,* vol. 86, no. 7, 2015.

[21] M. L. Hause, B. D. Prince and R. J. Bemish, "Krypton charge exchange cross sections for Hall effect thruster models," *Journal of Applied Physics,* vol. 113, no. 16, 2013.

[22] J. Fernandez-Coppel, R. Wirz and J. Marian, "Fully discrete model of kinetic ion-induced electron emission from metal surfaces," *Journal of Applied Physics,* vol. 135, no. 8, 2024.

[23] J. Dennison, C. Thomson, J. Kite, V. Zavyalov and J. Corbridge, "NASA Report No. 20040111058," 2004.

[24] H. Kawano, "Effective work functions for ionic and electronic emissions from mono- and polycrystalline surfaces," *Progress in Surface Science,* vol. 83, no. 1-2, pp. 1-165, 2008.

[25] H. D. Hagstrum, "Auger Ejection of Electrons from Tungsten by Noble Gas Ions," *Physical Review,* vol. 96, no. 2, pp. 325-335, 1954.

[26] L. Habi, D. Rafalskyi and T. Lafleur, "Ion beam diagnostic for the assessment of miniaturized electric propulsion systems," *Review of Scientific Instruments,* vol. 91, no. 9, 2020.

[27] S. G. Walton, J. C. Tucek, R. L. Champion and Y. Wang, "Low energy, ion-induced electron and ion emission from stainless steel: The effect of oxygen coverage and the implications for discharge modeling," *Journal of Applied Physics,* vol. 85, no. 3, pp. 1832-1837, 199.

[28] J. R. Beattie, "Numerical procedure for analyzing Langmuir probe data," *AIAA Journal,* vol. 13, no. 7, pp. 950-952, 1975.

Appendix

List of Acronyms:

- HAPC – Hidden Anode Plasma Contactor
- B-SPICE – Beam-Spacecraft Plasma Interaction and Charging Experiment
- E-beam – electron beam
- UoM – University of Michigan
- LANL – Los Alamos National Laboratory
- CSU – Colorado State University
- CEPPE – Center for Electric Propulsion and Plasma Engineering
- GIT – Gridded Ion Thruster
- HT - Hall Thruster
- HA – Hidden Anode
- HC – Hollow Cathode
- SSQ1 – science sequence 1
- SSQ2 – science sequence 2
- Aeq – Ampere equivalent
- COTS – commercial off the shelf
- pfc – proportional flow control valve
- PT – pressure transducer
- PID – proportional integral derivative
- pcb – printed circuit board
- HAHC – Hidden Anode Hollow Cathode
- sccm – standard cubic centimeters per minute

- CD – current density
- LP – Langmuir probe
- RPA – retarding potential analyzer
- ESA – Electrostatic analyzer
- E-VADER – Energy and Velocity Analyzer for Distributions of Electric Rockets
- E/q – energy per charge
- IISEE – Ion Induced Secondary Electron Emission
- IEDF – Ion Energy Distribution Function
- CAD – Computer Aided Design